



Quercetin and piperine enriched nanostructured lipid carriers (NLCs) to improve apoptosis in oral squamous cellular carcinoma (FaDu cells) with improved biodistribution profile

Vishal Sharad Chaudhari^a, Basveshwar Gawali^b, Pritam Saha^b, V.G.M. Naidu^{b, **},
Upadhyayula Suryanarayana Murty^c, Subham Banerjee^{a, *}

^a Department of Pharmaceutics, National Institute of Pharmaceutical Education and Research (NIPER)-Guwahati, Changsari, Kamrup, Assam, India

^b Department of Pharmacology and Toxicology, NIPER-Guwahati, Changsari, Kamrup, Assam, India

^c NIPER-Guwahati, Changsari, Kamrup, Assam, India

ARTICLE INFO

Keywords:

NLCs
Apoptosis
OSCC
FaDu cells
Biodistribution

ABSTRACT

Oral squamous cellular carcinoma (OSCC) is considered a life-threatening disease with detection in late stages, which forces us to opt for dangerous treatment with a combination of chemotherapy and radiotherapy. Herbal components such as piperine and quercetin are derived from edible sources, proving their anticancer potential against oral cancer cells *in vitro*. Encapsulation into lipid matrix-mediated nanostructured lipid carriers (NLCs) can make both drugs bio-accessible. NLCs were synthesised using the high shear homogenisation method and characterised for their physicochemical properties, followed by *in vitro* cellular evaluation in FaDu oral cancer cells. NLCs showed negatively charged particles smaller than 180 nm with a polydispersity index (PDI) of <0.3. Both drugs were found to encapsulate sufficiently, with >85% entrapment efficiency and an improved drug release profile compared to their pristine counterparts. Differential scanning calorimetry (DSC) thermograms showed conversion into an amorphous matrix in lyophilized NLCs, which was supported by X-ray diffraction (XRD) analysis. The cytotoxicity assay showed the IC₅₀ concentration for dual drug-loaded NLCs, which was more effective than the pure drug solution. NLCs were found to be internalised in cells in a short time with an almost 95% co-localization rate. Dual drug-loaded NLCs showed maximum depolarisation of the mitochondrial membrane along with more apoptotic changes. Improved apoptosis was confirmed in NLCs using flow cytometry. The *in vivo* biodistribution of Coumarin-6 labelled NLCs in rats confirmed their efficient distribution in various parts of the oral cavity through oral administration. Optimised dual drug-loaded NLCs provide a better option for delivering both drugs through a single lipid matrix against oral cancer.

1. Introduction

OSCC causes cancer in the epithelial tissues of the oral cavity of the mucosal lining. It accounts for almost 90% of all head and neck cancer cases (Lawoyin et al., 1996). It has been noticed that continuous and chronic usage of areca nut, tobacco, and betel quid leads to precancerous lesions in the oral cavity. The most affected areas are the oral squamous epithelial cells, tongue, gingiva, jaw bone, and lips (Wynder et al., 1957). The lack of techniques to detect early stage symptoms of OSCC is the main prognostic factor (Kulkarni, 2013). Chemotherapeutics and radiotherapy are preferred in cases where late-stage symptoms of OSCC

have been detected.

Nevertheless, several side effects have been observed associated with these advanced techniques, such as difficulty in swallowing, tooth decay, diminished salivary output (Cooper et al., 1995), ulceration in the mouth, sore throat, scar formation, and unusual bleeding. Dietary herbal components such as carotenoids, polyphenols, and many other components have been used to treat several diseases, either alone or in combination with two or more drugs. These drugs have the potential to cure many diseases with negligible side effects (Chaudhari et al., 2020a).

Quercetin is a potent antioxidant ubiquitously found in plants and various routinely consumed edibles, such as red onions and apples.

* Corresponding author.

** Corresponding author.

E-mail addresses: vgmnaidu@niperguwahati.ac.in (V.G.M. Naidu), subham.banerjee@niperguwahati.ac.in (S. Banerjee).

<https://doi.org/10.1016/j.ejphar.2021.174400>

Received 26 April 2021; Received in revised form 24 July 2021; Accepted 28 July 2021

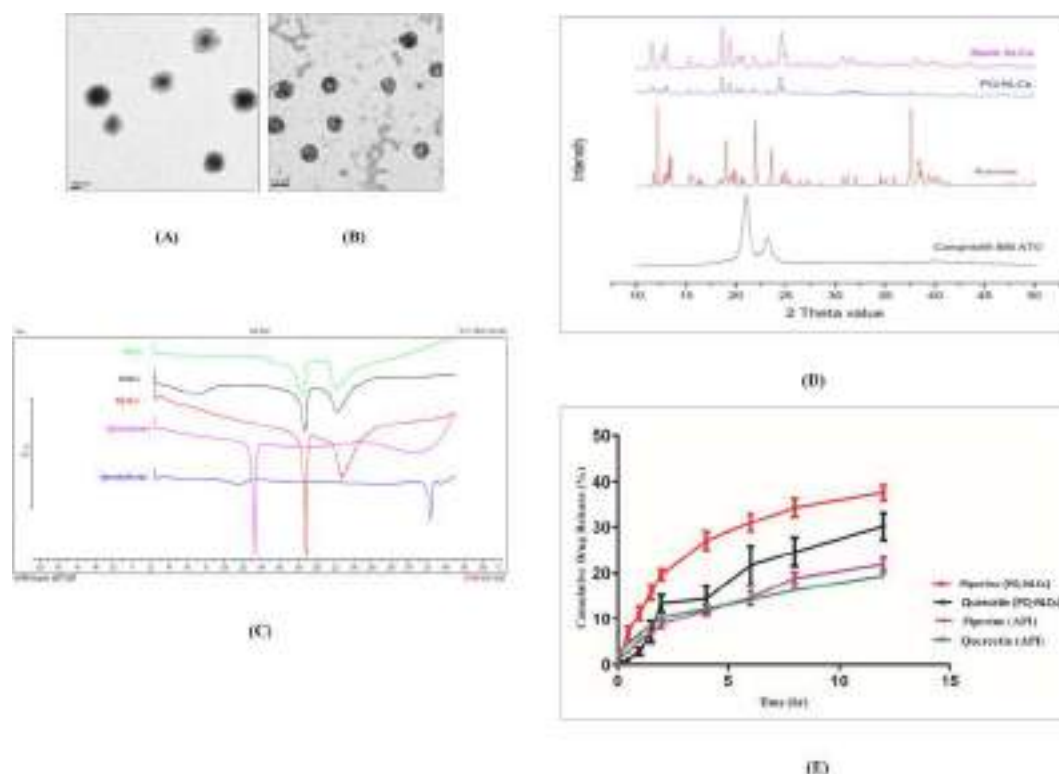
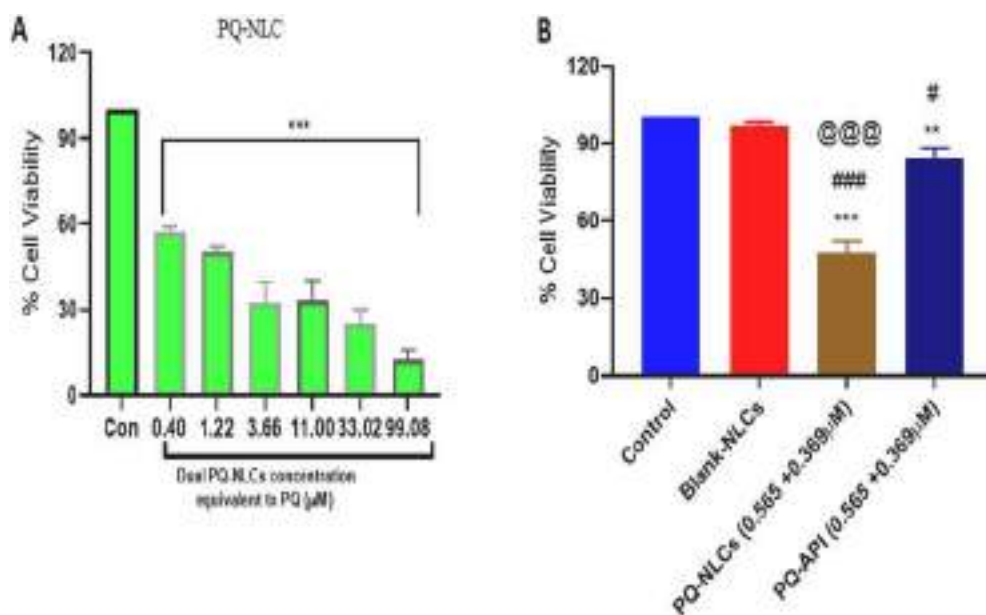
Available online 29 July 2021

0014-2999/© 2021 Elsevier B.V. All rights reserved.

Table 1

Particle size, PDI, and ZP values for prepared NLCs formulation.

| Formulation | Particle size (nm) | PDI | ZP (\pm mV) |
|-------------|--------------------|------------------|-------------------|
| Blank NLCs | 151.70 \pm 24.52 | 0.22 \pm 0.058 | -15.20 \pm 0.99 |
| PQ-NLCs | 128.10 \pm 32.02 | 0.16 \pm 0.050 | -17.06 \pm 4.73 |

Note: the results were expressed as mean \pm S.D (n = 6).**Fig. 1.** Physicochemical characterization of prepared NLCs. Images obtained from TEM as (A) Blank NLCs, (B) PQ-NLCs, (C) Thermograms obtained from DSC for all performed samples, (D) XRD pattern for all performed samples, and (E) *in-vitro* cumulative drug release (%) vs. time profile plot of pure API dispersions and PQ-NLCs releases.**Fig. 2.** Effect of PQ-NLCs on the viability of OSCC (FaDu cells). (A) Cells were treated with different concentrations of PQ-NLCs for 24 h. Cell viability was determined using MTT assay. Data were represented as Mean \pm SEM (n = 3). Statistical analyses were performed through one-way ANOVA followed by Dunnett's Test ***p < 0.001 V Control; and (B) Cells were treated with IC₅₀ concentration of PQ-NLCs for 24 h along with the equivalent concentration of individual API and blank NLCs. Values are presented as Mean \pm SEM (n = 3) and the comparisons are made on the basis of one-way ANOVA followed by Bonferroni multiple test, **P < 0.01, ***P < 0.001 vs control; #P < 0.01##P < 0.001 vs Blank; @@@P < 0.001 PQ-NLC vs PQ-API.

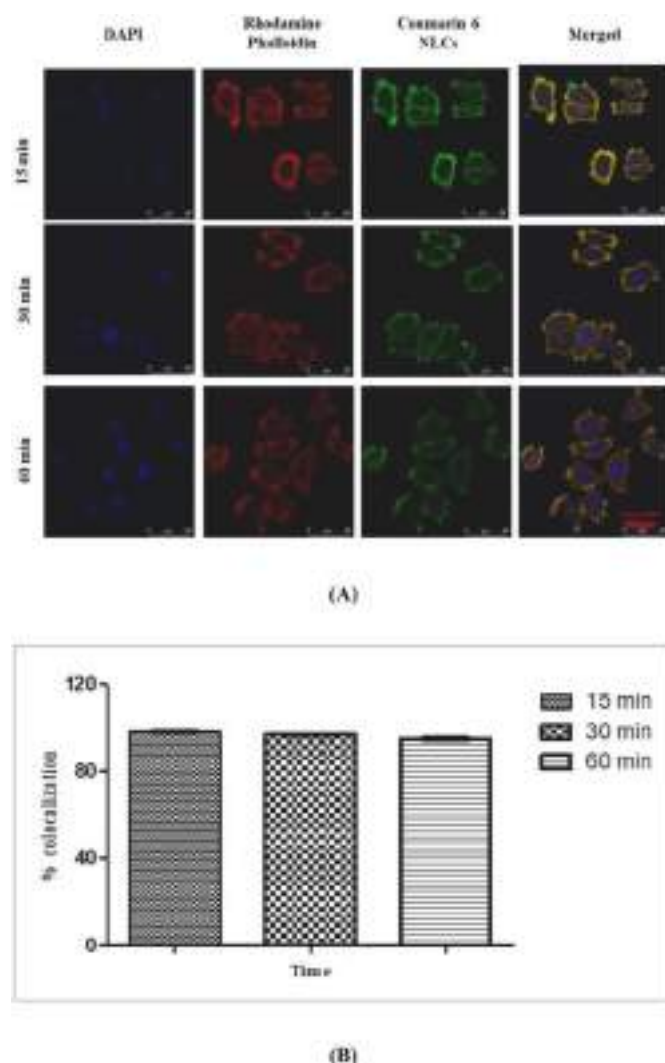


Fig. 3. Cellular internalization of NLCs. (A) CLSM images of Coumarin-6 labelled NLCs in FaDu cells; and (B) Plot of % co-localization vs. different time intervals of 15, 30, and 60 min.

(Siddiqui et al., 2017). Piperine has a high permeation rate because of its lipophilic and unionised nature and non-saturable absorption kinetics (Khajuria et al., 1998). Phytoconstituents such as quercetin and piperine have been widely explored in cancer cell lines, especially in oral cancer. Piperine has been found to inhibit p-glycoprotein efflux (Rather and Bhagat, 2018), hence it acts as a penetration-enhancing agent for other drugs. Both phytoconstituents act on different pathways in the prognosis of OSCC, which may give rise to new combination drugs from natural origin as a treatment. This provides a rationale for the combination treatment of OSCC. Several active constituents of plant origin have been successfully delivered through various lipid-based nanoformulations (Chaudhari et al., 2020b). Therefore, we aimed to incorporate the selected combination of both active constituents into NLCs and their characterization using several techniques, followed by *in vitro* cellular evaluation and biodistribution in rats.

2. Materials and methods

2.1. Materials

Compritol® 888 ATO, also known as glyceryl behenate, was obtained from Gattefosse, France. HPLC-grade acetonitrile, methanol, and glacial acetic acid were obtained from Merck Pvt. Ltd., Mumbai, India.

Squalene (SQL), a liquid lipid, piperine, quercetin, green, fluorescent Coumarin-6 dye, and dialysis sac with a molecular weight cut-off (MWCO) of 12 kDa were purchased from Sigma-Aldrich Chemical, St. Louis, MO. Emulsifiers such as Tween 80, Span 80, and acetone were purchased from HIMEDIA Laboratories Pvt. Ltd., Mumbai, India. Ethanol was purchased from EMSURE®Grade (Merck KGaA, Darmstadt, Germany). Water was purified with Milli-Q & ELIX, a water purification system (Merck Millipore, USA), and used throughout the experiments. Modified Eagle's medium (MEM), foetal bovine serum (FBS), penicillin, streptomycin, and trypsin/EDTA were purchased from Invitrogen Life Technologies, USA.

2.2. Methodology

2.2.1. Formulation development of NLCs

Solvent evaporation through high shear homogenisation followed by sonication was used to synthesise NLCs (Iqbal et al., 2012). Approximately 40% of Compritol® 888 ATO (solid lipid) along with 25% of SQL (liquid lipid) were solubilized in chloroform, followed by the addition of piperine (20%) and 2.5% Span 80 (Graves et al., 2015). Quercetin (10%) required acetone for solubilisation and was then transferred to the initial drug lipid mixture. After thorough mixing, the combined drug-lipid mixture was added slowly to an aqueous surfactant solution of Tween 80 (2.5%) under high shear homogenisation using a homogeniser (T25-D S22, IKA®, Germany) at constant rpm (15000 rpm) under cold conditions, followed by sonication using a probe sonicator (VCX500, SONICS Vibra cell, USA) with an amplitude of 20% and an on-off cycle of 8 and 12 s, respectively. Nano dispersion was filtered through Macrosep® 0.2 µm filter (Pall Corporation, Port Washington, NY) under centrifugation at 4 °C (Eppendorf Centrifuge 5810R, Germany). True nanoparticles of piperine and quercetin co-loaded NLCs (PQ-NLCs) were recovered from the filters. Blank NLCs were prepared without drugs using the procedure described above. Lyophilisation of the formulations was performed using sucrose as a cryoprotectant in a freeze dryer (L-300, Buchi, Switzerland). Previously reported sequential piperine-loaded NLCs (P-NLCs) and quercetin-loaded NLCs (Q-NLCs) were also prepared in a similar manner (Chaudhari et al., 2021) and used for comparison in cell line studies.

2.2.2. Characterization of NLCs

The properties of particles like hydrodynamic diameter, PDI, and zeta potential (ZP) of the prepared NLCs were characterised using a particle size analyser (Nano-ZS, Malvern Instruments Ltd.) at ambient room temperature. The surface morphological features of blank NLCs and PQ-NLCs were determined using transmission electron microscopy (TEM) (FEI Tecnai T20, Osaka, Japan) was used (Banerjee et al., 2020). The nature of the NLCs was studied using DSC (DSC-3, Mettler Toledo, Switzerland) and XRD (Bruker D8 Advance) (Banerjee et al., 2018).

2.2.3. Percent drug entrapment efficiency (%DEE) and drug loading (%DL)

NLC dispersions were filtered through a 3 kDa filter (Macrosep® Advance Centrifugal Device, Pall Corporation, Port Washington, NY) and centrifuged using an Eppendorf Centrifuge (5810R, Germany) at cold temperature, keeping a constant rpm of 3800 to remove the free drug. Retained particles were extracted from the entrapped drugs using a solvent mixture of acetone and chloroform (1:1). After vortexing, the organic layer was fractionated, filtered, and then analysed to quantify the encapsulated drug along with the free drug in the nanodispersion (Banerjee et al., 2018).

2.2.4. In-vitro drug release study and mechanism of drug release kinetics

The dialysis sac method was used to perform an *in vitro* drug release study for PQ-NLCs. Ethanolic solution (35% v/v) was used as the release medium. After sample withdrawal at different time intervals, sink conditions were maintained by replacing an equal volume of fresh release media. The samples were analysed by RP-HPLC method (Chaudhari

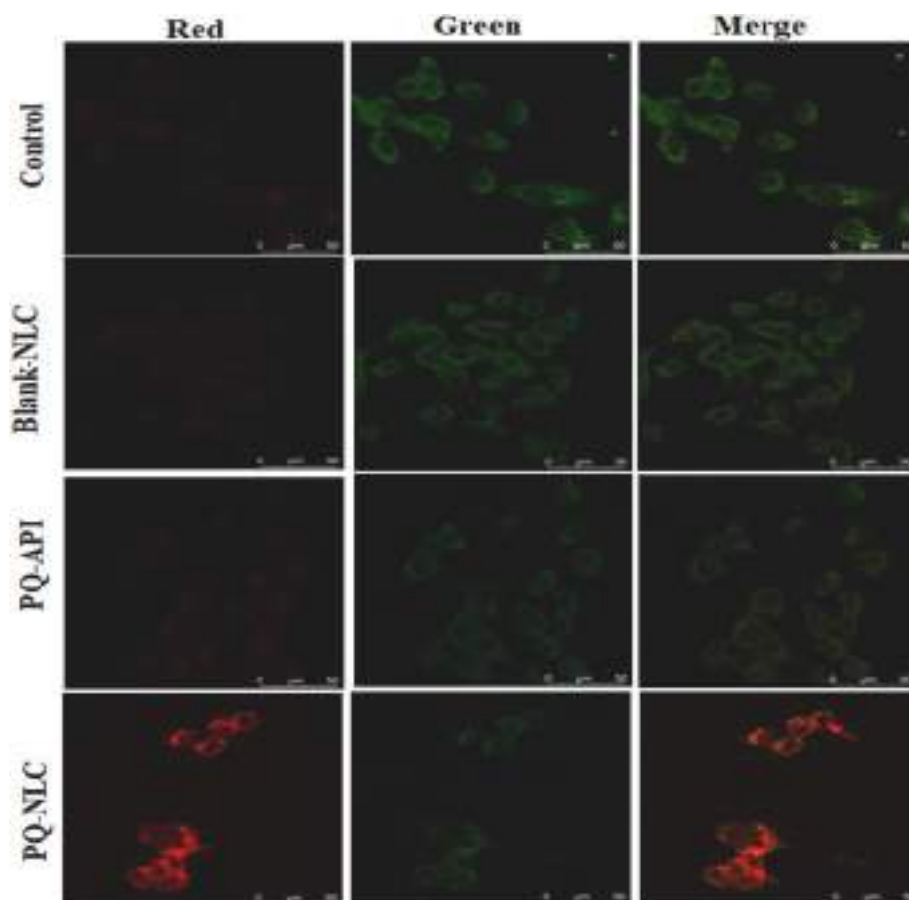


Fig. 4. Effect of PQ in API and NLCs form on apoptotic changes studied through dual AO/EtBr staining. Representative images of FaDu cells visualized under CLSM.

et al., 2020c). The release profile was plotted as % cumulative drug release versus time (h), and compared with the aqueous dispersion of the pristine active pharmaceutical ingredient (API). To determine the best fitting equations for release data, mathematical modelling of drug release kinetics was applied using relevant kinetics models, including zero-order, first-order, Higuchi, and Korsmeyer–Peppas models (Banerjee et al., 2018).

2.3. Cell culture conditions

FaDu cells (ATCC HTB-43; squamous cell carcinoma) were procured from the American Type Culture Collection (Manassas, VA, USA) and cultured in MEM medium supplemented with 10% FBS and penicillin-streptomycin. The cells were maintained in a humidified incubator at 37 °C with 5% CO₂ (HERACELL VIOS 150, Thermo Scientific). Cell lines were subcultured through enzymatic digestion with 0.25% trypsin/1 mM EDTA solution after reaching approximately 70 %–80% confluency.

2.3.1. Cytotoxicity assay

To determine the cytotoxic potential, 3-(4,5-dimethylthiazol-2-yl)-2,5-diphenyl tetrazolium bromide (MTT) assay was performed for optimised drug-loaded NLCs formulations and then compared with the combination of both drugs in their pristine solution form. FaDu cells (8×10^3) were seeded in 96 well sterile plates and treated with different concentrations of drugs for 24 h. NLCs were also compared to pure drugs in their individual forms. IC₅₀ values for NLCs formulations were determined against oral cancer cell lines after 24 h and used for further molecular analysis (Haghiac and Walle, 2005).

2.3.2. Internalization of NLCs

Coumarin-6 labelled NLCs were prepared similarly, as mentioned

earlier. FaDu cells were seeded on coated coverslips in 6-well plates and allowed to attach to the surface of the coverslip during an overnight incubation period. Then the treatment was given with fluorescent (coumarin-6) labelled NLCs for different time points of incubation 15 min, 30 min & 1 h (Banerjee et al., 2018, 2020). Images were acquired using a confocal laser scanning microscope (CLSM, TCS SP8, Leica Microsystems, Germany) in the blue, green, and red channels. All images were analysed using Leica LAS-X software.

2.3.3. Detection of apoptosis

The acridine orange (AO)/ethidium bromide (EtBr) staining technique was used to observe characteristic apoptotic morphological changes using CLSM. FaDu cells (1×10^5) were treated with IC₅₀ doses of NLCs formulations and pure drugs (equivalent concentrations of IC₅₀ dose NLCs) for 24 h. Morphological changes were observed by CLSM (Smith et al., 2012).

2.3.4. Identification of mitochondrial morphology through JC-1 dye

The alteration in mitochondrial membrane potential ($\Delta\Psi_m$) can be analysed using a confocal laser scanning microscope with the help of JC-1 dye. Cells were treated at doses with IC₅₀ NLCs formulations and for pure drugs (equivalent concentrations to IC₅₀ dose NLCs) incubated for 24 h followed by JC-1 dye. Images were captured using a CLSM (Nordin et al., 2019).

2.3.5. Annexin-V Fluorescein isothiocyanate (FITC) dot plot assay

Annexin-V FITC is a calcium-dependent phospholipid-binding protein with a high affinity for phosphatidylserine. It binds to apoptotic cells on an exposed cell surface. After treatment with NLCs, the cells were incubated with Annexin V FITC and propidium iodide (PI) for 20 min. Samples were diluted with 400 μ L binding buffer and analysed

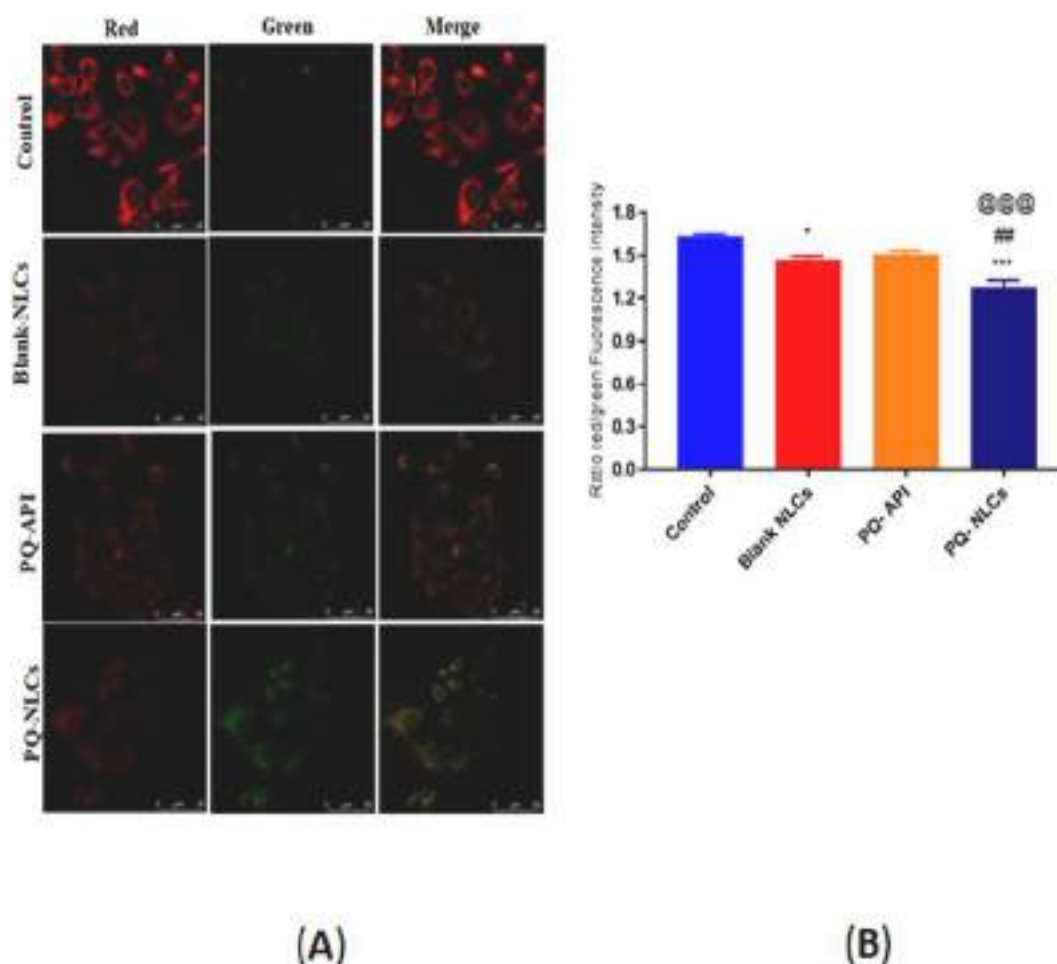


Fig. 5. Effect PQ in API and NLCs form on mitochondrial membrane potential ($\Delta\psi$). **(A)** Representative images of FaDu cells visualized under CLSM, and **(B)** Results were represented in the terms of the ratio of red/green fluorescence intensity. Values are presented as Mean \pm SEM ($n = 3$) and the comparisons are made based on one-way ANOVA followed by Bonferroni multiple tests, * $P < 0.05$, *** $P < 0.001$ vs Control; ## $P < 0.01$ vs Blank; @@@ $P < 0.01$ PQ-NLC vs PQ-API.

using a flow cytometer (Attune NXT software, Thermo Fisher Scientific, Singapore) (Nordin et al., 2019).

2.4. Biodistribution of Coumarin-6 labelled NLCs

Healthy Sprague Dawley (SD) rats (5–7 weeks of age, weighed between 220 and 250 g, either sex) were obtained from the Animal House Facility, National Institute of Pharmaceutical Education and Research (NIPER), Guwahati, Assam, India (IAEC Approval No.: NIPER/PE/19/24). Animals were acclimatised to the conditions and then kept deprived of food for 6 h before dosing Coumarin-6 labelled NLCs. At a dose volume of 5 ml/kg, Coumarin-6 labelled NLCs were administered through a per-oral route using oral gavage. After 6 h of dosing, animals were perfused with phosphate-buffered saline (PBS, pH 7.4) to remove the blood contaminant before organ collection, including the oral mucosa, tongue, and salivary gland. The organs were removed and washed with PBS (pH 7.4). For qualitative estimation, a portion of the tissue was sectioned using a cryotome (CMI1950UV, Leica) using tissue freezing media with a thickness of 5 μ m. Sections were mounted on a glass slide with an anti-fade reagent and then observed under a fluorescence microscope (EVOS FL Auto, Thermo Scientific). For quantification, approximately 100–150 mg of tissue was weighed from each organ, homogenised with methanol, and centrifuged at 13000 rpm for 10 min. The supernatant was used for dye quantification using Spectramax (i3X, Molecular Devices, USA) by measuring the fluorescence intensity (excitation at 457 nm and emission at 501 nm). The concentration of the

dye was expressed in ng/gm of tissue.

$$\text{Concentration of dye (ng/gm)} = \frac{\text{Concentration of dye (ng/ml)}}{\text{Weight of tissue (gm)}}$$

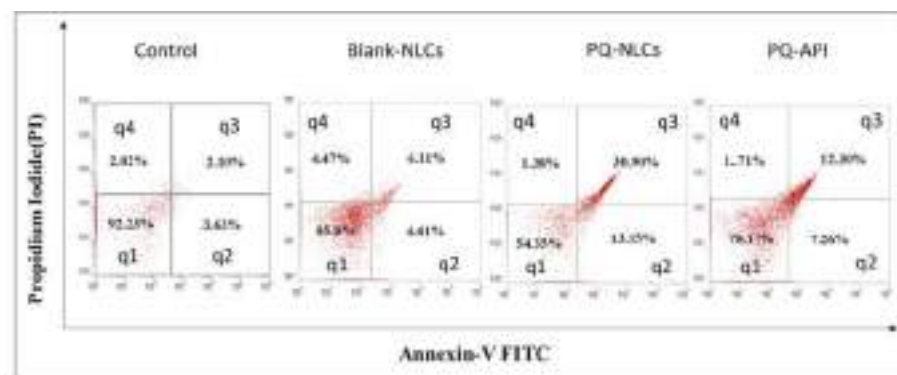
2.5. Statistical analysis

All values are expressed as the mean \pm standard deviation. Statistical analyses were performed using one-way analysis of variance (ANOVA) followed by Dunnett's test; *** $p < 0.001$ vs. control. The statistical significance between various groups of data was calculated and analysed using two-way ANOVA followed by Bonferroni's post-test. The criterion for statistical significance was set at $p < 0.05$. All statistical analyses were performed using Graph Pad Prism-8 (Graph Pad Software, San Diego, CA, USA).

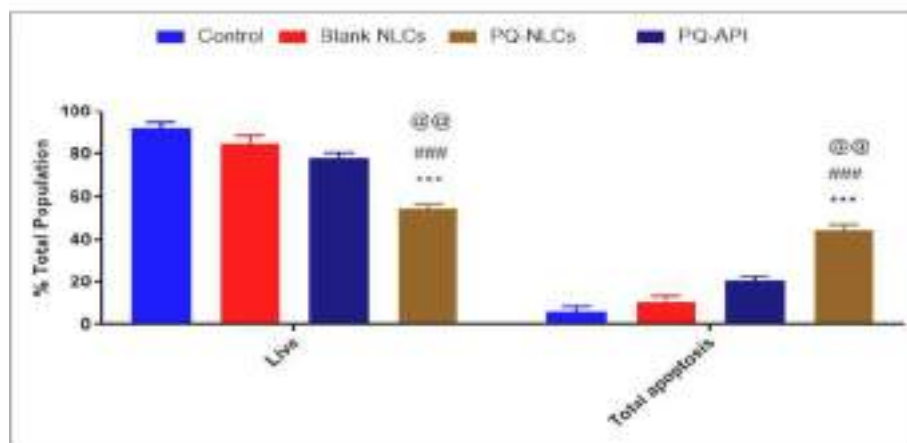
3. Results

3.1. Formulation characterizations

Dual drug-loaded NLCs and blank NLCs were analysed for particle size, PDI, and ZP using a particle size analyser, and the results are listed in Table 1. Particles prepared using this method were found to have particle sizes of less than 180 nm. An observed PDI < 0.3 , represented a highly monodispersed and homogenous population with a negative charge over the surface. TEM showed the smooth spherical shape of NLCs in agreement with data obtained from the particle size analyser in



(A)



(B)

Fig. 6. Effect PQ in API and NLCs form on the induction of apoptosis assessed by using Annexin-V FITC/PI. (A) Representative images from flow cytometry. Lower left Quadrant (q1): live cells; lower right quadrant (q2): early apoptosis; upper right quadrant (q3): late apoptosis; upper left quadrant (q4): necrotic cells, and (B) Results were expressed in the terms of % total population. Values are presented as Mean \pm SEM (n = 3) and the comparisons are made based on Two-way ANOVA followed by Bonferroni multiple tests, ***P < 0.001 vs Control; ###P < 0.001 vs Blank; @@P < 0.01 PQ-NLC vs PQ-API.

terms of size, which can be easily observed in Fig. 1(A) and 1(B). DSC thermograms depicted the absence of an endotherm for melting both drugs, as shown in Fig. 1(C). This explains the proper encapsulation of both drugs inside the lipid matrix in their converted amorphous form. This can be due to an increase in the surface area due to size reduction. Neither endotherm nor exotherm was observed in blank NLCs along with drug-loaded NLCs due to Compritol® 888 ATO as the lipid had already left its crystalline nature in the formulation and was converted into an amorphous form. The melting of sucrose around 185–190 °C followed by its degradation at around 220 °C was experienced earlier when used as a cryoprotectant in lipid nanoformulations (Jawad et al., 2018). XRD plots for blank NLCs and PQ-NLCs were obtained after XRD analysis, and the results are shown in Fig. 1(D). The presence of sharp, intense peaks in the XRD plot of NLCs mimics the peaks with sucrose, which was used as a cryoprotectant during lyophilisation. In addition, no other peaks were found in the NLCs along with the depression of the high-intensity peaks of Compritol® 888 ATO, indicating the amorphous conversion of both drugs along with solid lipids. Compared with the crystalline form, it is present either in the formulation or on the surface of PQ-NLCs; it is only due to sucrose.

3.2. % DEE and %DL

The liquid extraction method determined the % DEE and % DL for the optimised formulations (PQ-NLCs). The % DEE for piperine and quercetin from PQ-NLCs was found to be $88.30 \pm 4.16\%$ and $95.63 \pm$

1.38% , respectively. The % DL for piperine and quercetin was found to be $3.38 \pm 1.32\%$ and $1.04 \pm 0.48\%$, respectively, with six replicates.

3.3. In-vitro drug release study and mechanism of drug release kinetics

The dialysis sac method was used to analyse the *in vitro* release profiles of the dual-drug-loaded NLCs formulations. Cumulative drug release (%) was plotted against time (hr), as shown in Fig. 1(E). In the case of PQ-NLCs, quercetin was found to be released at 30% and piperine at 37.5%, which is higher than that of the pristine drug dispersion, which is less than that of PQ-NLCs. The mechanism of drug release for PQ-NLCs was determined by fitting the release study data to various mathematical models, as shown in Supplementary Table 1. According to the mechanism of drug release kinetics, drug-loaded NLCs were found to follow Higuchi release kinetics for quercetin ($R^2 = 0.9296$) and piperine ($R^2 = 0.9641$). This explains why the drug released from the NLCs followed the diffusion process.

3.4. Cytotoxicity assay

To determine the antitumor activity of dual drug-loaded NLCs on the growth of FaDu cells, IC_{50} values were measured using the MTT assay, as shown in Fig. 2(A), and it was found to be $0.934 \mu M$ for the prepared PQ-NLCs. The IC_{50} values were estimated at 24 h of exposure compared with the pristine drug, blank NLCs, and control, as shown in Fig. 2(B). The IC_{50} concentration of PQ-NLCs after 24 h was considered to be more

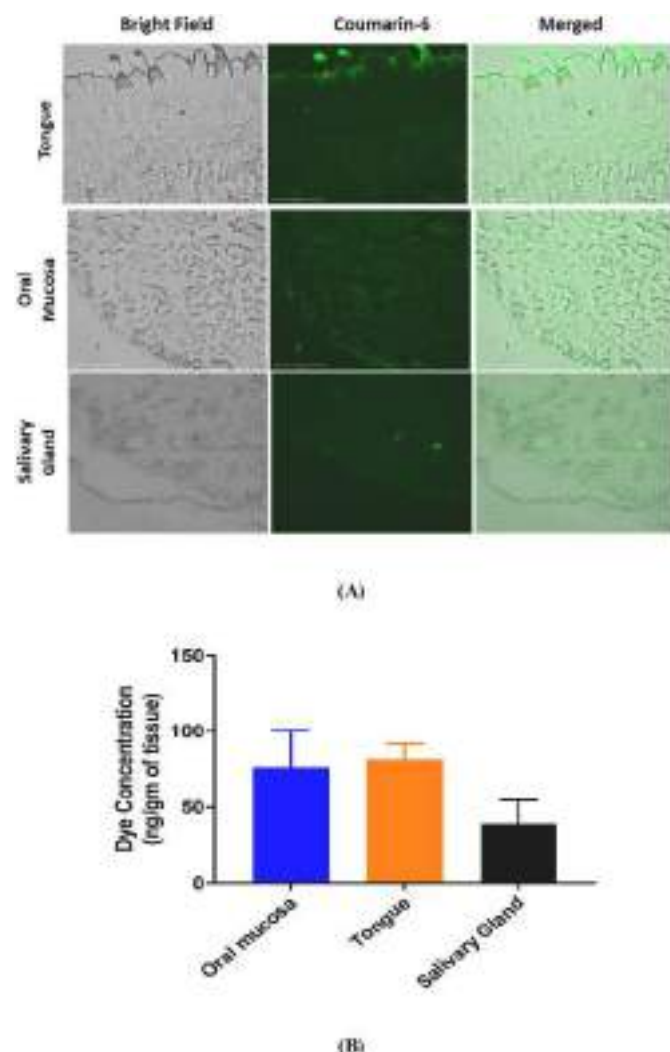


Fig. 7. Biodistribution profiles of Coumarin-6 labelled NLCs. (A) Fluorescence microscopic images of thin sections of various tissues obtained from SD rats after oral administration, visualized under fluorescence microscope, and (B) Quantification of Coumarin-6 (dye content in ng/gm of tissues) in respective oral tissues by measuring its fluorescence intensity.

toxic than that of the free drug combination in FaDu cells. The combination of pristine drugs at the IC₅₀ dose did not significantly reduce the viability percentage compared to control cells. The percentage of cell viability was significantly decreased in the case of PQ-NLCs exposed to FaDu cells, compared to control and the free combination drug-treated cells ($p < 0.001$). However, individual drug-loaded NLCs and their pristine drug solutions were also treated with cells for comparison. The plot for the cell viability assay for P-NLCs and Q-NLCs, along with their pure drug solutions, is shown in [Supplementary Fig. S1\(A\)](#) and [Fig. S1\(B\)](#). However, there were no significant changes in cell viability after treatment with Blank-NLCs compared to untreated cells.

3.5. Internalization of NLCs

Cellular uptake of nanoparticles is a crucial parameter to be determined after formulation development. Therefore, to understand the rate-dependent mechanism of cellular uptake of NLCs, coumarin-6 labelled NLCs were incubated with FaDu cells *in vitro*, as shown in [Fig. 3\(A\)](#). The images showed that particles were internalised within 15 min, with more than 95% co-localization, with a correlation coefficient of approximately 0.9524. Further, incubation of coumarin-6 labelled

NLCs with cells showed saturation of nanoparticles with almost similar percent co-localization, as shown in [Fig. 3\(B\)](#).

3.6. Detection of apoptosis through AO/EtBr staining

A confocal microscopic observation after 24 h of treatment with the IC₅₀ dose of PQ-NLCs on FaDu cells stained with AO/EtBr depicts both early and late apoptotic features such as chromatin condensation, membrane blebbing, the formation of apoptotic bodies, and fragmented nuclei. Staining with AO/EtBr confirmed apoptotic changes in FaDu cells induced after treatment with PQ-NLCs ([Fig. 4](#)). For comparison purposes, P-NLCs and Q-NLCs were also performed for this assay along with their pure drug solution, and the images are shown in [Supplementary Fig. S2](#).

3.7. Identification of mitochondrial morphology through JC-1 dye

JC-1 is a cationic dye that is used to determine mitochondrial depolarisation and mitochondrial membrane potential. Treatment with IC₅₀ dose PQ-NLCs increased JC-1 monomer in cells, which was observed in confocal microscopic images, resulting in increased green fluorescence intensity, suggesting apoptotic mitochondrial depolarisation ($\Delta\psi$), as shown in [Fig. 5\(A\)](#) and [Fig. 5\(B\)](#). The treatment was also given at IC₅₀ concentrations of the sequential formulation along with their pure drug solution, and images are shown in [Supplementary Fig. S3\(A\)](#). At the same time, the fluorescence intensity plot is presented in [Supplementary Fig. S3\(B\)](#). Drug-loaded formulations caused more mitochondrial depolarisation than pure drug solutions. Dual drug-loaded NLCs showed a lower fluorescence intensity ratio than the others, indicating maximum depolarisation of the mitochondrial membrane, leading to cell death. Blank NLCs also showed mitochondrial depolarisation to some extent compared to the control.

3.8. Annexin-V FITC dot plot assay

Flow cytometric analysis was used to determine apoptosis using annexin-V FITC and PI dual staining. Flow cytometric analysis indicated that after 24 h of treatment with IC₅₀ PQ-NLCs on FaDu cells significantly increased the percentage of late apoptosis and early apoptosis compared to untreated cells, and treated with respective free drug concentrations, as shown in [Fig. 6\(A\)](#) and [Fig. 6\(B\)](#). However, no significant changes were observed in the percentage of total apoptotic cells exposed to blank-NLCs. Necrotic indices of FaDu cells were not significantly altered in response to the IC₅₀ dose of P-NLCs or Q-NLCs [[Supplementary Fig. S4\(A\)](#) and [Fig. S4\(B\)](#)], and PQ-NLCs, along with an equivalent concentration of the free drug.

3.9. In-vivo biodistribution of NLCs

The utilisation of coumarin-6 dye-labelled nanoparticles to determine the *in vivo* fate of nanoparticles in biodistribution has been studied earlier. It was observed that Coumarin-6 labelled NLCs were found to reach almost all organs, including the tongue, salivary gland, and oral mucosa, as evident from the microscopic image of tissue sections and quantification of Coumarin-6 dye in the respective tissues by measuring the fluorescence intensity using Spectramax i3X, as shown in [Fig. 7\(A\)](#). The concentration of dye was determined by the intra-polation method using the standard curve concentration ranging from 4.88 to 625 ng/ml, and the concentration of dye in tissue samples was quantified in terms of fluorescence intensity, as shown in [Fig. 7\(B\)](#). In addition, particles in oral tissues, such as the oral mucosa, salivary glands, and tongue, reach the regions of the buccal cavity. It can be used as an effective treatment for oral cancer.

4. Discussion

Solvent evaporation through the high-shear homogenisation method was implemented for the synthesis of NLCs. Compritol® 888 ATO, a solid lipid, makes nanoparticles rigid while SQL, a liquid lipid, prevents the crystallisation of solid lipids through an anomalous structure of the lipid matrix. A lower lipid concentration allows proper distribution of sonication energy throughout the nanodispersion and yields a lower particle size (Das et al., 2012). The role of the surfactant is critical in reducing the particle size because of the reduced surface tension, which prevents the coalescence of particles in the nanodispersion (Hu et al., 2004). The reduced particle size increases the surface area and improves permeation through the GI membrane, thereby facilitating absorption through the lymphatic system (Li et al., 2017). Lower PDI values were obtained because of the higher surfactant concentration and utilisation of Compritol® 888 ATO (Das et al., 2012). The negative charge over the nanoparticle surface explains the repulsion between particles in the nanodispersion, preventing the aggregation of NLCs (Freitas and Müller, 1999). Owing to the presence of liquid lipids and solid lipids, the inner structure became anomalous.

In addition, drugs are encapsulated inside the lipid matrix with higher entrapment efficiency, as demonstrated by TEM. The XRD results resembled the DSC plot, as both techniques confirmed the conversion of drugs in amorphous form during their encapsulation inside the lipid matrix. This confirmed the absence of drugs on the surface of the NLCs. The presence of liquid lipids prevents *in-situ* crystallisation of solid lipids. This causes the matrix to be anomalous; hence, higher drug encapsulation can be expected in the case of NLCs (Müller et al., 2002). Piperine (log P: 3.38) was more lipophilic than quercetin (log P = 1.81). This allowed piperine to encapsulate within the lipid matrix significantly more significantly than quercetin when administered in combination.

In addition, Compritol® 888 ATO, a solid lipid solubilized in chloroform only, and piperine also showed solubility in the same solvent, while quercetin was not soluble in it. Due to its higher lipophilicity and solubility, piperine showed more release than quercetin from PQ-NLCs. In addition, the rigidity obtained in NLCs due to Compritol® 888 ATO leads to slower diffusion of drugs from the lipid matrix (Zhang et al., 2014). Higher drug encapsulation in NLCs followed slow diffusion of the drug from tiny liquid nano-compartments of more profound parts of the solid-liquid lipid matrix with a longer diffusion distance (Müller et al., 2002). This explains why the drug released from the NLCs followed the diffusion process.

It has been reported that the IC₅₀ value for quercetin is approximately 50 µM when treated against the SSC-9 cell line (Haghiac and Walle, 2005), while piperine showed an IC₅₀ value of 124 µM against the KB cell line (Siddiqui et al., 2017). Interestingly, blank NLCs displayed apoptosis potential to some extent, as observed in the JC-1 assay, by altering the mitochondrial membrane potential. Reports have suggested that SQL exhibits anticancer properties via perturbed mitochondrial membrane potential (Palaniyandi et al., 2018). As SQL, we used it as an integral component of NLCs, so we can infer that the mitochondria-mediated apoptosis inducing potential is due to the presence of SQL. Combining both drugs in a single NLCs matrix showed a synergistic effect with improved cytotoxic potential. Overall, the results showed that the formulation showed a higher cytotoxic potential at a lower concentration than the pristine drug solutions. The rate and extent of particle uptake generally depend on the physicochemical characteristics of the particles, including their size, ZP, and shape. Stable uptake of nanoparticles, followed by degradation by lysosomal enzymes, causes the release of drugs encapsulated within the lipid matrix. Colour intensity reflects higher colocalization with no background. The formulations showed more apoptotic changes than the pure drug solutions. Dual drug-loaded NLCs showed more early and late apoptotic changes in all treatments. The decrease in red fluorescence intensity and increase in green fluorescence intensity indicates mitochondrial depolarisation due

to the opening of the mitochondrial permeability transition pore (MPTP) due to the loss of intracellular accumulation of J-aggregates and increase in their monomeric form (green). This leads to mitochondrial membrane disruption and loss of function. Annexin V FITC and PI dual staining were used to quantify the necrotic indices in FaDu cells using flow cytometry. Quantitative estimation has been studied in tissues by determining the dye concentration, and qualitative evaluation through fluorescence imaging using fluorescence microscopy (Chu et al., 2018).

In conclusion, dual drug-loaded NLCs prepared by encapsulation of quercetin and piperine were characterised for their particle properties, including size, PDI, and ZP. In addition, microscopic evaluation revealed drug encapsulation within the lipid matrix. The improved drug release profile was obtained using NLCs as compared to the pristine drugs. Both drug-encapsulated NLCs proved to be more cytotoxic than pristine drug solutions, with faster cell internalization. Cellular apoptosis assays showed an increase in apoptosis in the oral cancer cell lines. The *in vivo* biodistribution of Coumarin-6 labelled NLCs in rats confirmed the efficient distribution in oral cavity parts, which is essential for the treatment of oral cancer. The overall scenario predicts an improvement in the activity of both drugs after encapsulation in NLCs. There is scope for further *in vivo* assessment of these optimised NLCs in terms of exploring pharmacokinetics and pharmacodynamic studies.

Funding

This work was funded by the National Mission on Himalayan Studies [File No: GBPI/NMHS-2017-18/HSF-02], Ministry of Environment, Forest and Climate Change, Govt. of India.

CRediT authorship contribution statement

Vishal Sharad Chaudhari: Data curation, Formal analysis, Investigation, Methodology, Validation, Visualization, Writing – original draft. **Basveshwar Gawali:** Data curation, Formal analysis, Investigation, Methodology, Validation, Visualization, Writing – original draft. **Pritam Saha:** Data curation, Formal analysis, Investigation, Methodology, Validation, Visualization, Writing – original draft. **V.G.M. Naidu:** Conceptualization, Formal analysis, Resources, Supervision, Validation, Visualization, Writing – review & editing. **Upadhyayula Suryanarayana Murty:** Funding acquisition, Project administration, Resources. **Subham Banerjee:** Conceptualization, Formal analysis, Resources, Supervision, Validation, Visualization, Writing – review & editing.

Declaration of competing interest

There are no conflicts to declare.

Acknowledgments

We acknowledge the National Mission on Himalayan Studies (NMHS), Ministry of Environment, Forest and Climate Change, Govt. of India to provide the necessary funding support for this research work. Authors are also thankful to the Department of Pharmaceuticals, Ministry of Chemicals and Fertilisers, Govt. of India. We would also like to acknowledge the North-East Centre for Biological Sciences and Healthcare Engineering (NECBH), IIT Guwahati, and the Department of Biotechnology (DBT), Govt. of India for Powder XRD instrumentation facility.

Appendix A. Supplementary data

Supplementary data to this article can be found online at <https://doi.org/10.1016/j.ejphar.2021.174400>.

References

- Banerjee, S., Roy, S., Bhaumik, K.N., Pillai, J., 2020. Mechanisms of the effectiveness of lipid nanoparticle formulations loaded with anti-tubercular drugs combinations toward overcoming drug bioavailability in tuberculosis. *J. Drug Target.* 28, 55–69. <https://doi.org/10.1080/1061186X.2019.1613409>.
- Banerjee, S., Roy, S., Nath Bhaumik, K., Kshetrapal, P., Pillai, J., 2018. Comparative study of oral lipid nanoparticle formulations (LNFs) for chemical stabilization of antitubercular drugs: physicochemical and cellular evaluation. *Artif. Cells Nanomed. Biotechnol.* 46, 540–558. <https://doi.org/10.1080/21691401.2018.1431648>.
- Chaudhari, V.S., Murty, U.S., Banerjee, S., 2020a. Lipidic nanomaterials to deliver natural compounds against cancer: a review. *Environ. Chem. Lett.* 18, 1803–1812. <https://doi.org/10.1007/s10311-020-01042-5>.
- Chaudhari, V.S., Hazam, P.K., Banerjee, S., 2020b. Lipid nanoarchitectonics for natural products delivery in cancer therapy, *Sustainable Agriculture Reviews*, vol. 44. Springer, pp. 169–203. https://doi.org/10.1007/978-3-030-41842-7_5.
- Chaudhari, V.S., Borkar, R.M., Murty, U.S., Banerjee, S., 2020c. Analytical method development and validation of reverse-phase high-performance liquid chromatography (RP-HPLC) method for simultaneous quantifications of quercetin and piperine in dual-drug loaded nanostructured lipid carriers. *J. Pharmaceut. Biomed. Anal.* 186, 113325. <https://doi.org/10.1016/j.jpba.2020.113325>.
- Chaudhari, V.S., Murty, U.S., Banerjee, S., 2021. Nanostructured Lipid Carriers as a strategy for encapsulation of active plant constituents: formulation and in vitro physicochemical characterizations. *Chem. Phys. Lipids* 235, 105037. <https://doi.org/10.1016/j.chemphyslip.2020.105037>.
- Chen, S.F., Nien, S., Wu, C.H., Liu, C.-L., Chang, Y.C., Lin, Y.S., 2013. Reappraisal of the anticancer efficacy of quercetin in oral cancer cells. *J. Chin. Med. Assoc.* 76, 146–152. <https://doi.org/10.1016/j.jcma.2012.11.008>.
- Chu, L., Wang, A., Ni, L., Yan, X., Song, Y., Zhao, M., Sun, K., Mu, H., Liu, S., Wu, Z., 2018. Nose-to-brain delivery of temozolomide-loaded PLGA nanoparticles functionalized with anti-EPHA3 for glioblastoma targeting. *Drug Deliv.* 25, 1634–1641. <https://doi.org/10.1080/10717544.2018.1494226>.
- Cooper, J.S., Fu, K., Marks, J., Silverman, S., 1995. Late effects of radiation therapy in the head and neck region. *Int. J. Radiat. Oncol. Biol. Phys.* 31, 1141–1164. [https://doi.org/10.1016/0360-3016\(94\)00421-G](https://doi.org/10.1016/0360-3016(94)00421-G).
- Das, S., Ng, W.K., Tan, R.B., 2012. Are nanostructured lipid carriers (NLCs) better than solid lipid nanoparticles (SLNs): development, characterizations and comparative evaluations of clotrimazole-loaded SLNs and NLCs? *Eur. J. Pharmaceut. Sci.* 47, 139–151. <https://doi.org/10.1016/j.ejps.2012.05.010>.
- Freitas, C., Müller, R., 1999. Correlation between long-term stability of solid lipid nanoparticles (SLNTM) and crystallinity of the lipid phase. *Eur. J. Pharm. Biopharm.* 47, 125–132. [https://doi.org/10.1016/S0939-6411\(98\)00074-5](https://doi.org/10.1016/S0939-6411(98)00074-5).
- Graves, R.A., Ledet, G.A., Nation, C.A., Pramart, Y.V., Bostanian, L.A., Mandal, T.K., 2015. Effect of squalene on mebendazole-loaded Compritol® nanoparticles. *J. Biomater. Sci. Polym. Ed.* 26, 868–880. <https://doi.org/10.1080/09205063.2015.1061351>.
- Haghiaci, M., Walle, T., 2005. Quercetin induces necrosis and apoptosis in SCC-9 oral cancer cells. *Nutr. Canc.* 53, 220–231. https://doi.org/10.1207/s15327914nc5302_11.
- Hu, L., Tang, X., Cui, F., 2004. Solid lipid nanoparticles (SLNs) to improve oral bioavailability of poorly soluble drugs. *J. Pharm. Pharmacol.* 56, 1527–1535. <https://doi.org/10.1211/0022357044959>.
- Iqbal, M.A., Md, S., Sahni, J.K., Baboota, S., Dang, S., Ali, J., 2012. Nanostructured lipid carriers system: recent advances in drug delivery. *J. Drug Target.* 20, 813–830. <https://doi.org/10.3109/1061186X.2012.716845>.
- Jawad, R., Elleman, C., Martin, G.P., Royall, P.G., 2018. Crystallisation of freeze-dried sucrose in model mixtures that represent the amorphous sugar matrices present in confectionery. *Food. Funct.* 9, 4621–4634. <https://doi.org/10.1039/c8fo00729b>.
- Khajuria, A., Zutshi, U., Bedi, K., 1998. Permeability characteristics of piperine on oral absorption-an active alkaloid from peppers and a bioavailability enhancer. *Indian J. Exp. Biol.* 36, 46–50. <https://pubmed.ncbi.nlm.nih.gov/9536651/>.
- Kulkarni, M.R., 2013. Head and neck cancer burden in India. *Int. J. Head Neck Surg.* 4, 29–35. <https://doi.org/10.5005/jp-journals-10001-1132>.
- Lawoyin, J., Lawoyin, D., Aderinokun, G., 1996. Intra-oral squamous cell carcinoma in Ibadan: a review of 90 cases. *Afr. J. Med. Med. Sci.* 26, 187–188. <https://pubmed.ncbi.nlm.nih.gov/10456168/>.
- Li, Q., Cai, T., Huang, Y., Xia, X., Cole, S.P., Cai, Y., 2017. A review of the structure, preparation, and application of NLCs, PNPs, and PLNs. *Nanomaterials* 7, 122. <https://doi.org/10.3390/nano7060122>.
- Ma, Y.S., Yao, C.N., Liu, H.C., Yu, F.S., Lin, J.J., Lu, K.W., Liao, C.L., Chueh, F.S., Chung, J.G., 2018. Quercetin induced apoptosis of human oral cancer SAS cells through mitochondria and endoplasmic reticulum mediated signaling pathways. *Oncol. Lett.* 15, 9663–9672. <https://doi.org/10.3892/ol.2018.8584>.
- Müller, R., Radtke, M., Wissing, S., 2002. Nanostructured lipid matrices for improved microencapsulation of drugs. *Int. J. Pharm.* 242, 121–128. [https://doi.org/10.1016/S0378-5173\(02\)00180-1](https://doi.org/10.1016/S0378-5173(02)00180-1).
- Nordin, N., Yeap, S.K., Rahman, H.S., Zambari, N.R., Abu, N., Mohamad, N.E., How, C. W., Masarudin, M.J., Abdullah, R., Alitheen, N.B., 2019. In vitro cytotoxicity and anticancer effects of citral nanostructured lipid carrier on MDA MBA-231 human breast cancer cells. *Sci. Rep.* 9, 1–19. <https://doi.org/10.1038/s41598-018-38214-x>.
- Palaniyandi, T., Sivaji, A., Thiruganasambandam, R., Natarajan, S., Hari, R., 2018. In Vitro antitumor activity of squalene, a triterpenoid compound isolated from *Rhizophora mucronata* mangrove plant leaves against AGS cell line. *Phcog. Mag.* 14, 369. <https://www.phcog.com/article.asp?issn=0973-1296;year=2018;volume=14;issue=57;page=369;epage=376;aulast=Palaniyandi;type=0>.
- Rather, R.A., Bhagat, M., 2018. Cancer chemoprevention and piperine: molecular mechanisms and therapeutic opportunities. *Front. Cell Dev. Biol.* 6, 10. <https://doi.org/10.3389/fcell.2018.00010>.
- Siddiqui, S., Ahamad, M.S., Jafri, A., Afzal, M., Arshad, M., 2017. Piperine triggers apoptosis of human oral squamous carcinoma through cell cycle arrest and mitochondrial oxidative stress. *Nutr. Canc.* 69, 791–799. <https://doi.org/10.1080/01635581.2017.1310260>.
- Smith, S.M., Ribble, D., Goldstein, N.B., Norris, D.A., Shellman, Y.G., 2012. A simple technique for quantifying apoptosis in 96-well plates. *Methods Cell Biol.* 112, 361–368.
- Wynder, E.L., Bross, I.J., Feldman, R.M., 1957. A study of the etiological factors in cancer of the mouth. *Cancer* 10, 1300–1323. [https://doi.org/10.1002/1097-0142\(195711/12\)10:6<1300::aid-cnrc2820100628>3.0.co;2-2](https://doi.org/10.1002/1097-0142(195711/12)10:6<1300::aid-cnrc2820100628>3.0.co;2-2).
- Zhang, C., Peng, F., Liu, W., Wan, J., Wan, C., Xu, H., Lam, C.W., Yang, X., 2014. Nanostructured lipid carriers as a novel oral delivery system for triptolide: induced changes in pharmacokinetics profile associated with reduced toxicity in male rats. *Int. J. Nanomed.* 9, 1049. <https://doi.org/10.2147/IJN.S55144>.

3D PRINTING OF BIOMEDICAL MATERIALS AND DEVICES



Fused deposition modeling (FDM)-mediated 3D-printed mouth-dissolving wafers loaded with nanostructured lipid carriers (NLCs) for in vitro release

Vishal Sharad Chaudhari¹, Tushar Kanti Malakar¹, Upadhyayula Suryanarayana Murty², Subham Banerjee^{1,a)} 

¹Department of Pharmaceutics, National Institute of Pharmaceutical Education and Research (NIPER)-Guwahati, Kamrup, Assam, India

²NIPER-Guwahati, Changsari, Kamrup, Assam 781 101, India

^{a)}Address all correspondence to this author. e-mail: banerjee.subham@yahoo.co.in

Received: 16 April 2021; accepted: 24 June 2021

Localized delivery of drugs or nanoparticles for oral cancer is always preferred. Additive manufacturing (AM)-driven 3D-printed wafers to deliver nanoparticles offers a new dimension to the cutting-edge delivery perspective. Nanostructured lipid carriers (NLCs) were loaded inside 3D wafers, printed using poly (vinyl alcohol) as polymer. Wafers showed a loading capacity of 50 ± 2.5 mg with desired surface and unaltered thermal properties. In vitro release of NLCs was performed to ascertain the release of particles from 3D wafer. Derived Kilo Counts per Second (KCPS) obtained from dynamic light scattering (DLS) corresponds to NLCs population. The progressive release of NLCs from 3D wafer was observed in a time-dependent manner as the PVA matrix became exhausted and started dissolving in artificial saliva, leading to the release of complete NLCs. Thus, NLCs delivery through 3D wafers at the desired site of action can be considered the latest AM-driven treatment approach for oral cancer.

Introduction

3D printing is an innovative technology for the fabrication of three-dimensional objects using a computer-aided design (CAD) file. Fused deposition modeling (FDM)-mediated 3D printing follows layer-by-layer printing to provide a 3D structure for the designed object [1]. 3D printing has been developed in the pharmaceutical field in terms of personalized medicine, medical devices, tissue engineering, oral dosage forms, and other drug delivery prototypes [2]. FDM works with the principle of melting the polymer filament and extruding the materials in 3D-printed format over the build platform. It is a type of subsequent melting and cooling of thermoplastic materials and deposition onto the build plate in a layer-by-layer deposition manner [3]. Based on the literature, polyvinyl alcohol (PVA) is one of the most promising polymers in the field of 3D printing because of its ideal thermoplastic properties, solubility in water, and used as a support material in complex designs through extrusion-mediated 3D printing. In addition, it is a colorless, odorless, non-toxic, biodegradable thermoplastic polymer with good thermal stability [4]. This polymer has been widely used as a drug carrier in

pharmaceuticals [5–8]. Thus, the design and prototyping of a 3D-printed wafer may be an innovative idea with the blessing of this versatile biodegradable polymer that can open up a new dimension in delivering drug and/or particle to the buccal cavity for localized disease treatment such as oral cancers.

Nanostructured lipid carriers (NLCs) have been explored as delivery systems for natural active plant constituents with enhanced bioavailability and improved activity [9]. Active plant constituent-enriched NLCs have also been explored with enhanced efficacy against cancer treatment and are well summarized in our earlier article [10]. In our previous study, active plant constituent-enriched NLCs were successfully developed and validated [11], but it requires cutting-edge translational dosage format to deliver the cargo in terms of both particles and drugs at a local site in the buccal cavity. However, the delivery of NLCs in their lyophilized form through biodegradable cum mouth-dissolvable 3D-printed wafers is not done so far. This would be an excellent value addition to the AM-driven innovative dosage form against oral cancer mitigation through a localized drug delivery approach.

To ascertain the proper delivery of NLCs from a 3D wafer, the dynamic light scattering (DLS) technique is chosen as a sophisticated, reliable technique for not only the determination of particle size in their nanorange but also comes with an additive tool of estimating derived kCPS (kilo Counts per Second) of particle populations present in NLCs, which corresponds to the concentration of nanoparticles [12, 13]. Hence, the current research work focuses on quantifying particles released from NLCs using the DLS technique to predict the particle in vitro release behavior from a 3D wafer. Therefore, we aimed to design a prototype by PVA filament-derived 3D-printed wafers using the FDM technique along with its physicochemical validations. Further, these printed 3D wafers are characterized to determine their delivery potential to release the particles from NLCs in terms of both qualitative & quantitative particle release rate manners.

Results

Design and printing of 3D wafers

Computer-aided design (CAD) designs of the 3D wafers are shown in Fig. 1. To print wafers as a 3D object, an FDM-mediated 3D printer was implemented, and a natural, high-quality PVA filament was used as the polymer. Printing parameters such as printing temperature, printing speed, and layer height were varied in different batches, as shown in Table 1. The optimized wafers were further characterized using various techniques.

Preparation and characterizations of NLCs

Nanostructured lipid carriers were prepared using a method similar to that previously reported earlier [11]. All excipients used in the formulation of NLCs are generally regarded as safe (GRAS)-certified materials. The particle size and polydispersity index of the prepared NLCs were characterized again using a particle size analyzer. NLCs were found to have a size of less than 100 nm with a PDI value < 0.3. This ensured a highly monodisperse population of NLCs present in the nanodispersion. The

TABLE 1: Process variations in 3D printing parameters.

| Wafer code | Printing parameters | | |
|------------|---------------------------|-----------------------|-------------------|
| | Printing temperature (°C) | Printing speed (mm/s) | Layer height (mm) |
| W1 | 215 | 70 | 0.1 |
| W2 | 215 | 70 | 0.15 |
| W3 | 215 | 80 | 0.1 |
| W4 | 215 | 80 | 0.15 |
| W5 | 225 | 70 | 0.1 |
| W6 | 225 | 70 | 0.15 |
| W7 | 225 | 80 | 0.1 |
| W8 | 225 | 80 | 0.15 |

particle size distribution plot of NLCs dispersion is shown in Fig. 2. Lyophilisation of NLCs was performed using sucrose as a cryoprotectant and utilized in other evaluations, including in vitro particle release study.

Characterization of 3D wafers

Physical appearance

The 3D wafer had a rectangular shape with a slightly rough surface at the edges and smooth flat surfaces. Both flat surfaces were slightly shiny, as shown in Fig. 3.

Physical dimensions

As per the aforementioned protocol, all batches of 3D-printed wafers in the assembled form were measured for their thickness, length, and width in millimeter and their values are listed in Table 2. The thickness for 3D-printed wafers was found to be in the range of 4.81 ± 1.23 mm to 5.4 ± 0.24 mm, while the length was 21.47 ± 0.22 mm to 21.84 ± 0.04 mm, and width was 11.65 ± 0.32 mm to 11.98 ± 0.1 mm. All values showed almost no significant differences in terms of their average values against different printing process parameters.

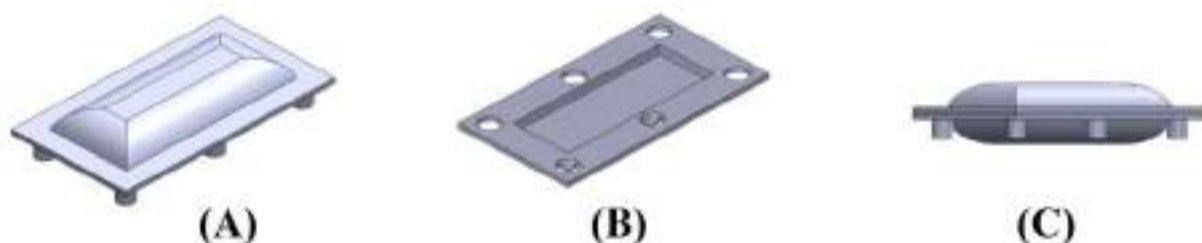


Figure 1: Computer-aided design (CAD) for the 3D-printed wafer. It mainly consists of two parts, where (a) top part, which is having 6 projections on its outer part, (b) bottom part is having 6 holes on its outer part, and (c) Combined wafer assembly is comprised of fixation of part A and part B in each other through projections and wells, respectively.

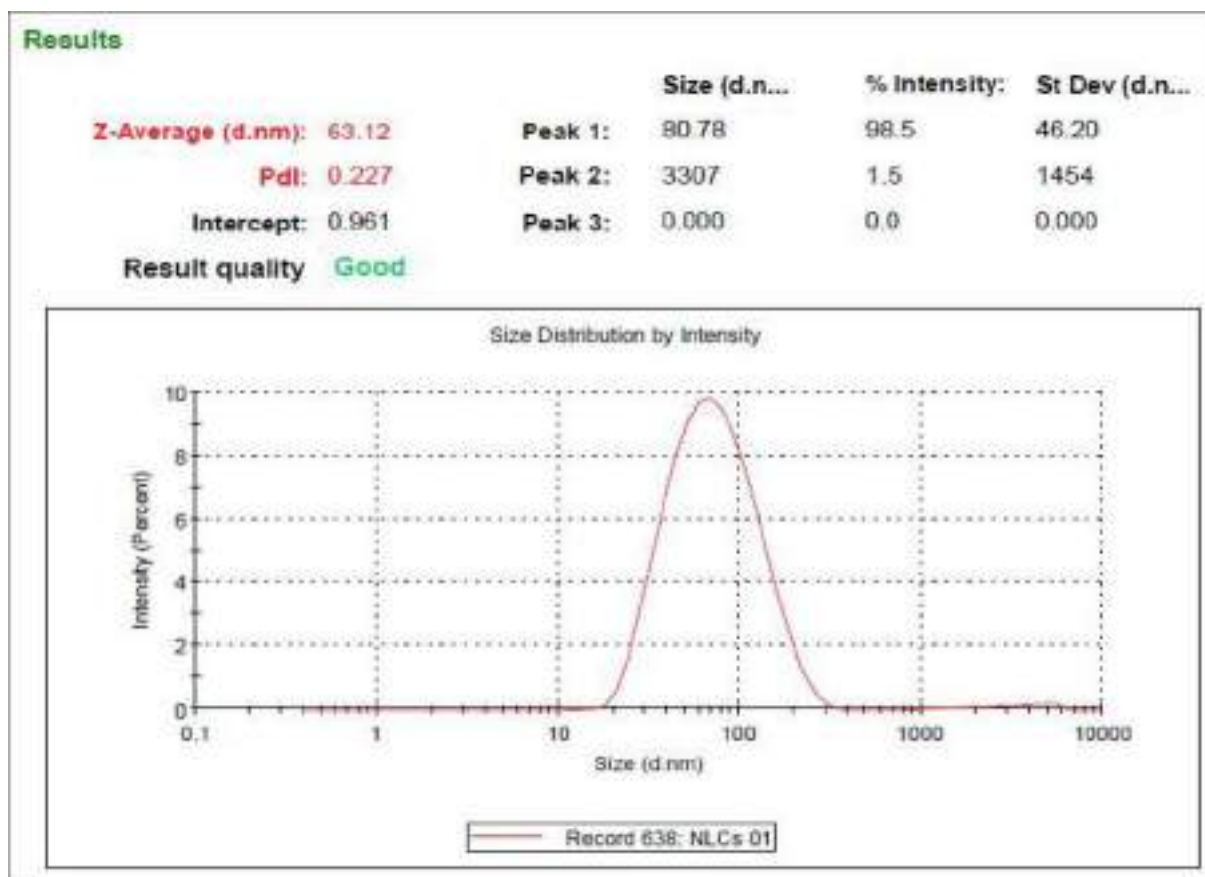


Figure 2: Particle size distribution plot for NLCs obtained from particle size analyzer. The mean particle size distribution along with the PDI value represents the monodisperse particle population.

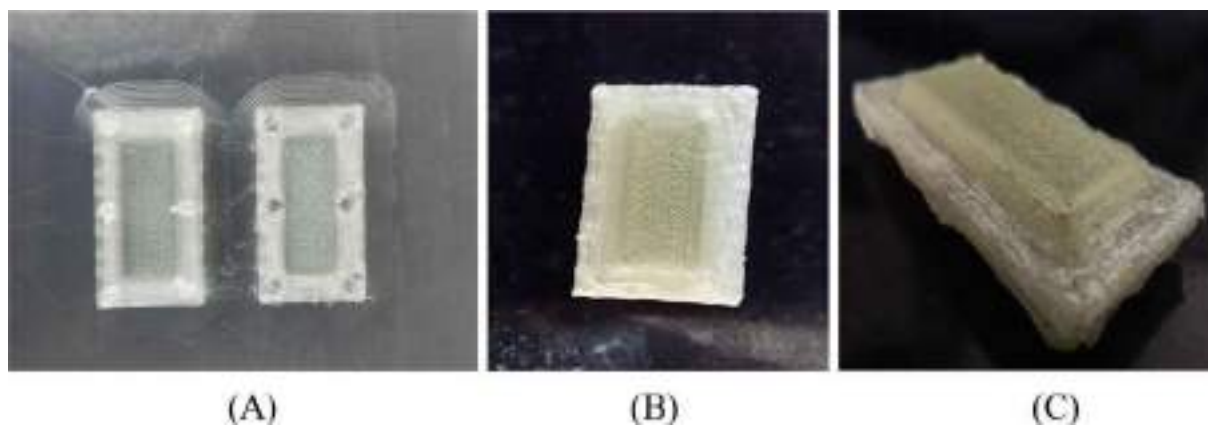


Figure 3: Various images of 3D-printed wafers (a) two parts of the wafer (left: bottom part & right: top part), (b) complete wafer assembly (Side view), (c) complete wafer assembly (Perspective view), respectively.

Weight variation

The weight variation in different batches of 3D wafers was studied to determine the variations in the printability of 3D printers. Wafers from all batches were weighed in six replicates, and

the average weights (\pm SD) for different batches are displayed in Table 2. All wafers were found to be in the weighing range between 474.95 ± 39.43 mg to 577.40 ± 10.51 mg. This reflects the light weight nature of the wafer and can be easily held in the oral cavity.

TABLE 2: Evaluation of different printing process parameters.

| Wafer code | Evaluation parameters | | | |
|------------|--------------------------|-----------------------------|--------------------------|-------------------------|
| | Weight (mg) ^a | Thickness (mm) ^a | Length (mm) ^a | Width (mm) ^a |
| W1 | 565.90 (± 10.85) | 5.07 (± 0.09) | 21.84 (0.04) | 11.86 (0.05) |
| W2 | 577.40 (± 10.51) | 5.23 (± 0.08) | 21.47 (± 0.22) | 11.75 (± 0.08) |
| W3 | 525.98 (± 29.57) | 5.20 (± 0.11) | 21.70 (± 0.08) | 11.80 (± 0.15) |
| W4 | 474.95 (± 39.43) | 5.40 (± 0.24) | 21.49 (± 0.26) | 11.65 (± 0.32) |
| W5 | 534.52 (± 17.38) | 4.81 (± 1.23) | 21.81 (± 0.05) | 11.88 (± 0.12) |
| W6 | 517.53 (± 22.28) | 5.26 (± 0.13) | 21.65 (± 0.17) | 11.68 (± 0.3) |
| W7 | 553.63 (± 7.18) | 5.07 (± 0.15) | 21.84 (± 0.04) | 11.98 (± 0.1) |
| W8 | 515.78 (± 12.11) | 4.97 (± 0.19) | 21.50 (± 0.22) | 11.83 (± 0.07) |

^aAll data represents Mean (± SD), n = 6.

Selection of 3D wafer

We found insignificant differences among all batches based on the properties evaluated for 3D wafers with variations in the printing parameters. These variations in terms of weight, thickness, length, and width, along with their physical appearance through visual inspection, were almost negligible, leading to the inability to segregate these different batches of wafers. This describes the uniformity in the printability of the FDM-based 3D printing of wafers. Hence, we selected only one of these for further evaluation.

Loading capacity

The loading capacity of the 3D wafers was determined manually but accurately, filling the lyophilized NLCs inside the wafers. Approximately 50 ± 2.5 mg of lyophilized NLCs can quickly be loaded inside the 3D wafers. This is sufficient for the loading capacity for localized dosing and delivery of NLCs in a lyophilized format. This large amount of lyophilized active plant constituents enriched NLCs loading inside the 3D wafer can be ensured to be delivered without any leakage or spillage. Hence, the developed 3D wafers can be a good option for localized delivery of NLCs inside the oral cavity against oral cancer.

Microscopy of 3D wafers

To determine the surface morphology and structure of the 3D wafer, a microscopic evaluation was performed under an inverted microscope, as shown in Fig. 4. Images obtained from an optical microscope proved the layered structure of the printing, leading to a smooth surface of the 3D wafer. Layer-by-layer printing of natural PVA filaments using an FDM printer can be easily observed from microscopic images.

SEM

Field emission (FESEM) imaging was performed for NLCs, as in a lyophilized product format, as shown in Fig. 5a. As the particle

size was significantly smaller, the lyophilized particles required a high resolution for imaging. FESEM confirmed the nanostructured size of the NLCs. The surface morphology of the NLCs was found to be slightly rough and anomalous in nature. This does not reflect the complete spherical shape of the NLC particles. The addition of sucrose as a cryoprotectant induces the sticky nature of NLCs, which was observed due to the agglomeration of a few particle populations. The surface texture of the particles was relatively smooth, with no crystalline drug events observed.

The FESEM images of the 3D wafers are shown in Fig. 5b. The surface of the wafer exhibited gridline architecture with low roughness. This also indicates that the presence of minipores or minivoids might be due to irregularities during the printing process but with the maintenance of structural integrity of the prototyped 3D-printed wafer.

DSC

DSC analysis was performed to determine the nature of the PVA filament in the pre-printing form and the 3D wafer after post-printing the PVA filament. The DSC thermograms obtained for all samples are shown in Fig. 6. The PVA filament showed an endothermic peak around 185–190 °C with its decomposition at 320 °C. A similar pattern of thermal signature was also observed for the 3D wafer. This suggests that no significant changes occurred before and after printing the native natural PVA filaments. Therefore, no drastic effect occurred through the extrusion of the PVA polymer at approximately 215–225 °C during printing. Such a similar observation was also experienced by our research group [8].

XRD analysis

The XRD plots for both the PVA filament and 3D wafer are shown in Fig. 7. The plot suggests a lack of high-intensity peaks showing no crystalline structure in either the PVA filament or 3D wafer. Interestingly, the intensity decreased in the 3D wafer compared to that in the PVA filament. This is due to the thermal shock to the filament during melting extrusion, followed

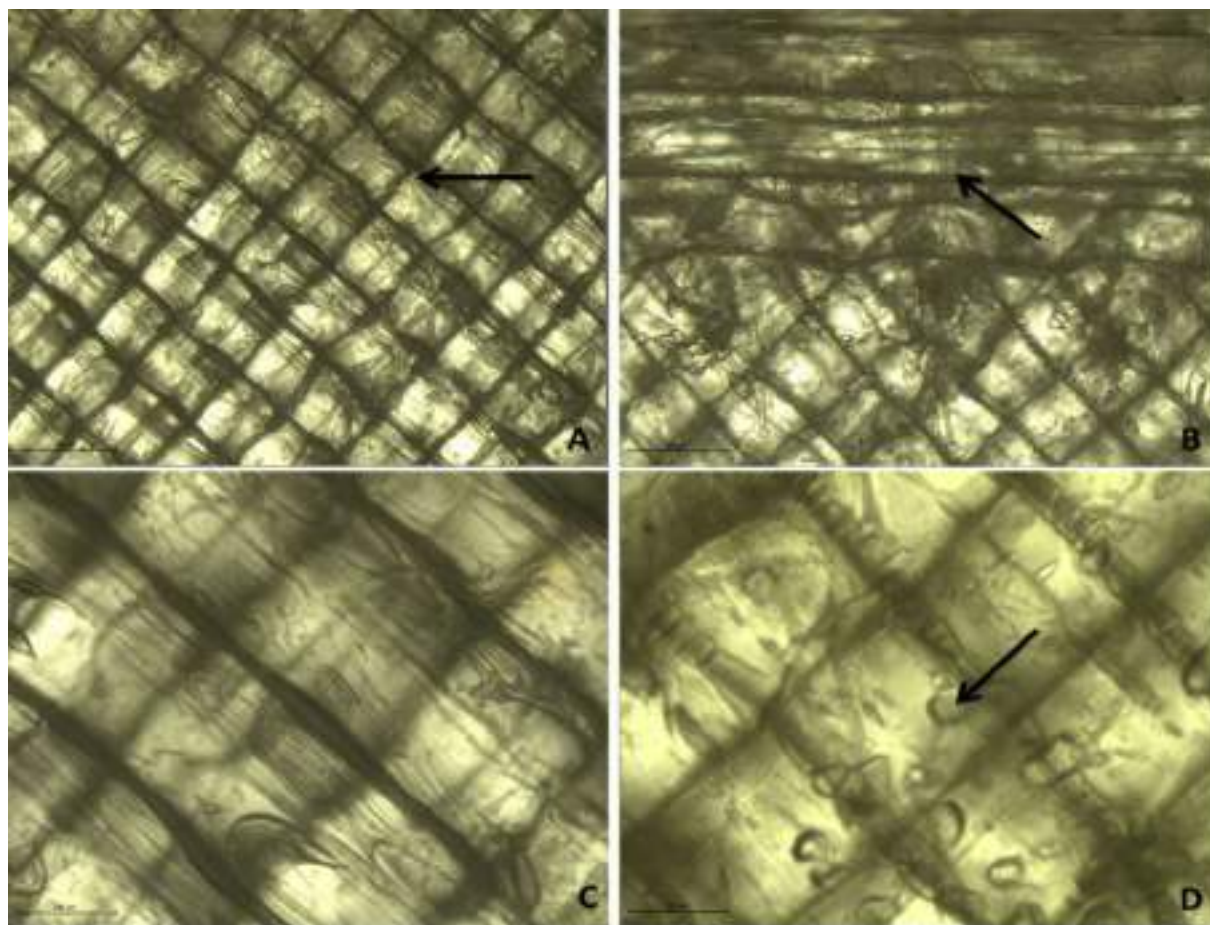


Figure 4: Microscopic images of 3D-printed wafers representing layer-by-layer printing structure from FDM-3D printer with the presence of minipores over the surface highlighted by an arrow.

by consolidation into a 3D-printed wafer structure. Therefore, both materials are non-crystalline and amorphous in solid-state geometry.

Determination of % redispersibility of NLCs

The percent redispersibility of NLCs is an essential determinant of lyophilized products. The study was performed in a context with a significant focus on the kCPS derived for NLCs. Hence, the % redispersibility was also measured in terms of the derived kCPS and was found to be $104.67\% \pm 1.68$ when lyophilization and reconstitution were performed in Milli-Q water in triplicate of the NLCs sample.

In vitro NLCs release study

An in vitro particle release study was performed on NLCs loaded into 3D wafers in artificial saliva as a dissolution medium. The particle concentration was estimated using the DLS-based derived kCPS values. In this experiment, the release of particles from 3D wafers was estimated in artificial saliva at various time points using DLS in a similar way [12]. The final value of

particle release was estimated by subtracting the derived kCPS values of the blank 3D wafer and the derived kCPS values of artificial saliva from the derived kCPS of NLC-loaded 3D wafers. The time taken for the progressive release of NLCs from the 3D wafer was plotted on the x-axis against the derived kCPS of particles on the y-axis, as shown in Fig. 8. Particle size distribution plot measured by DLS technique from NLCs loaded 3D wafer at different time intervals, i.e., 30 min, 60 min, 90 min, and 120 min, was displayed in Fig. 9. The complete time-dependent release of NLCs from 3D wafers occurred within 120 min, and hence can be helpful in the delivery of nanoparticles inside the buccal cavity.

Discussion

FDM-mediated 3D printing technology has reached a milestone in the field of drug delivery and pharmaceuticals. It provides flexibility to fabricate complex geometries and further integrate [14]. Hence, the implementation of 3D wafers to deliver NLCs provides a new dimension to the particle delivery perspective.

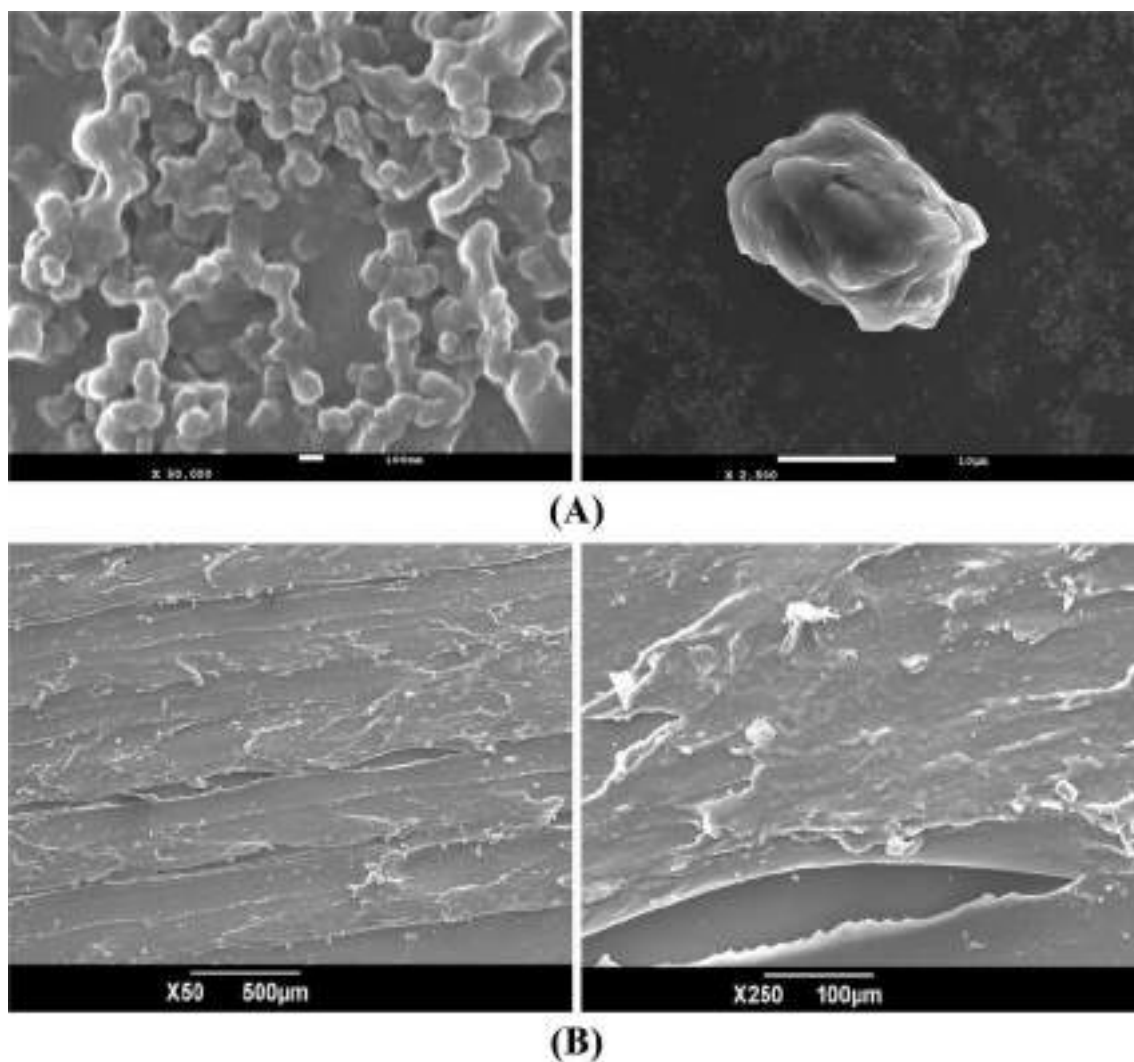


Figure 5: SEM micrographs for NLCs and 3D-printed wafer. (a) Lyophilized NLCs, representing clusters of particles due to aggregation during the process of lyophilization. Also, the SEM images of single-particle exhibit rough surface structure and (b) 3D wafer observed under different magnifications signifies the presence of layer-by-layer printed structure, irregular rough surfaces with the formation of small voids/pores.

It can deliver particles at the desired sites of action in a more localized manner and is further dissolvable owing to the biodegradable nature of native polymeric filaments. Thus, the overall study was projected to integrate NLCs with FDM-mediated 3D-printed wafers to deliver the particles justifying their buccal delivery applications.

Initially, the 3D wafer was designed using CAD software and printed using fused deposition modeling (FDM)-mediated 3D printing technology. The PVA filament is a transparent, flexible, and smooth filament with an average diameter of 2.85 mm and is used for prototyping a 3D wafer. The variations in the printing process parameters of the 3D wafers did not show any significant differences in their physical dimensions, weight, and printability. This reflects the robustness of the prototyped 3D wafer. The wafers showed a loading capacity of 50 ± 2.5 mg of lyophilized

NLCs, which reflects sufficient space to load the particles inside it without any leakage or spillage with proper tight fixation. This provides the delivery of NLCs in a lyophilized format, where reconstitution is not required. The squares can be seen from the microscopic evaluations simply reflecting the layer-by-layer printing nature of 3D wafers with a shiny surface. The presence of minipores over the surfaces can provide space for saliva to erode the wafer and make the way available for the desired particle release. Similar results were obtained from scanning electron microscopy (SEM), where grid lines of structures with slight roughness and microstructural pores were also observed. This could play a crucial role in wafer dissolution. It predicts erosion followed by a diffusion-type release pattern owing to its surface.

In addition, SEM showed a cluster of nanosized particles due to sucrose as a cryoprotectant with anomalousness and a

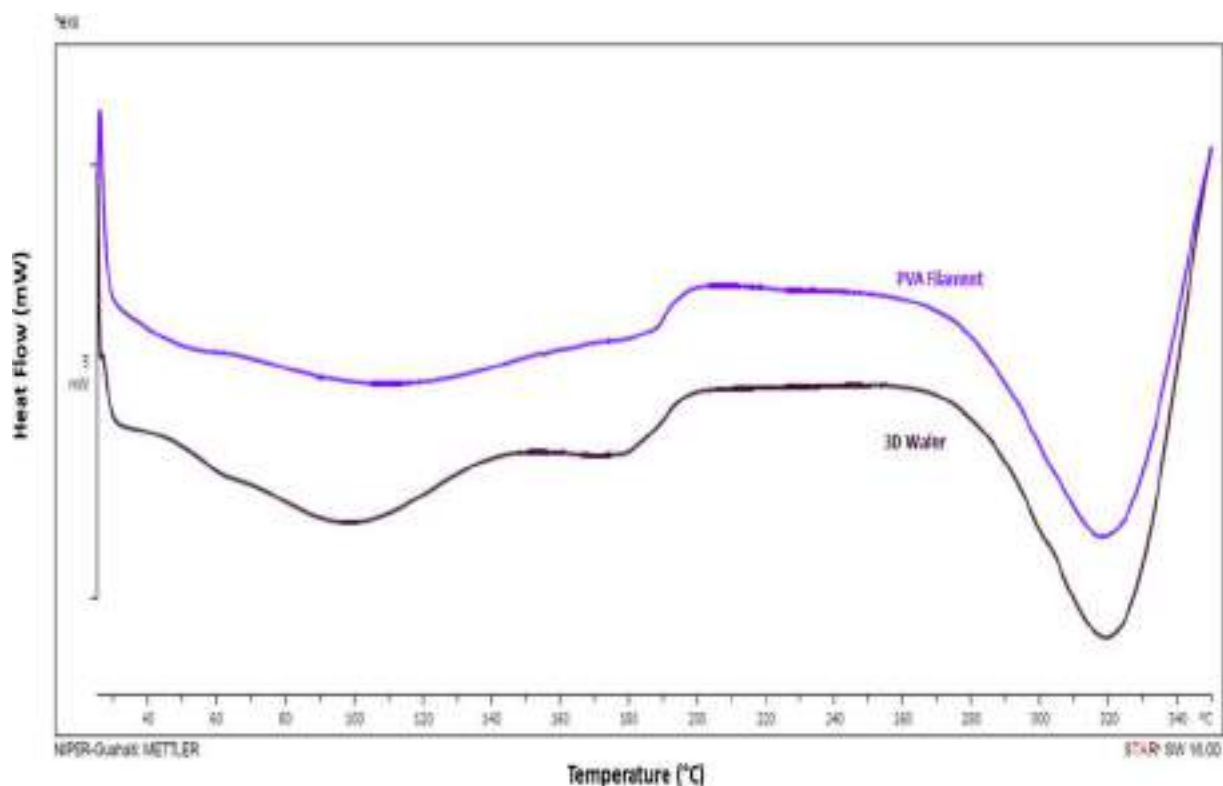


Figure 6: DSC thermograms for 3D wafer and PVA filament, predicting the thermal stability behavior of PVA filament both in native form and post 3D printing process.

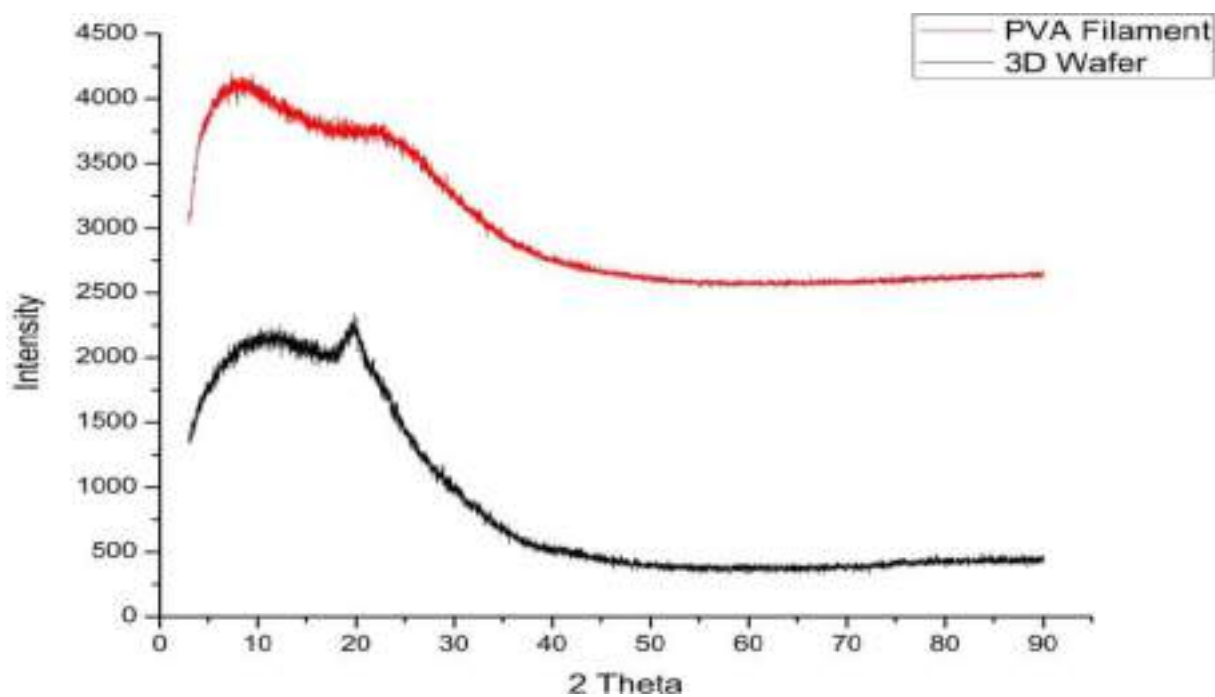


Figure 7: XRD pattern for 3D wafer and PVA filament for the solid-state prediction of material in terms of either crystalline or amorphous.

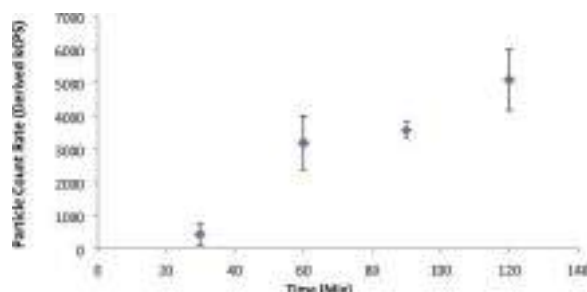


Figure 8: Plot of in vitro NLCs release from NLCs loaded 3D wafer as plotted in respect to particle count rate (derived kCPS) versus time in min.

slightly rough surface of particles. The DSC curve showed no drastic effect on the PVA before and after extrusion through the hot nozzle of the FDM-3D printer. The native PVA filament showed melting around 185–190 °C followed by drastic degradation around 320 °C; hence, we restricted the printing temperature to approximately 215–225 °C to avoid degradation of the object, as observed previously [5]. There were no sharp, intense Bragg peaks observed in the XRD plot with a slight reduction

in the intensity of the PVA filament compared to the 3D wafer [15]. A very recent report published by our research group for the fabrication of a 3D-printed compartmental delivery system for anti-tubercular drugs through print and fill strategy showed the utilization of PVA polymer and its potential implication as a 3D-printed housing device. The PVA polymers did not show any significant variations in their DSC and XRD patterns before and after 3D printing [8].

The concept of derived kCPS to determine the population of NLCs present in the nanodispersion is an innovative approach that has not been explored as such. Hence, we quantified the NLC population count rate from the prepared nanodispersions. The redispersibility of lyophilized NLCs reflects easy reconstitution with an almost similar concentration of NLCs. The critical application of this method was to estimate the NLC particle population count rate from 3D-printed wafer matrix system. It was found to release complete NLCs within 120 min, as quantified from the derived kCPS concept. In a previous publication, the release of polymeric nanocapsules from 3D-printed tablets was studied qualitatively, where nanocapsules released from the 3D-printed tablets were determined through particle size distribution plots by DLS estimation [12].

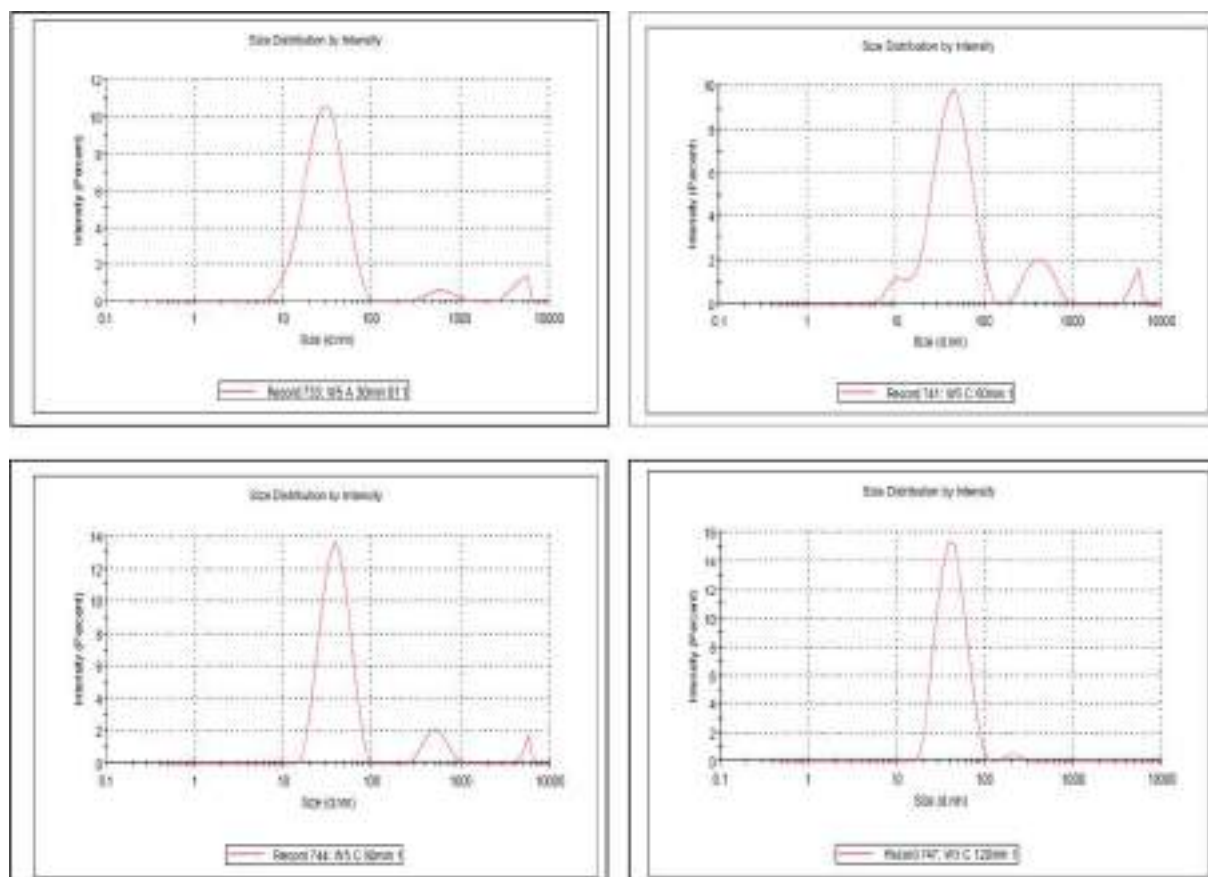


Figure 9: Particle size distribution plot by DLS analysis of NLCs loaded 3D wafer at different time intervals, i.e., 30 min, 60 min, 90 min, and 120 min.

Nevertheless, the present work represents a quantification approach regarding the derived kCPS count rate for releasing NLCs from 3D-printed PVA wafers. The mechanism of particle release may be predicted as initial wetting of the 3D wafer followed by diffusion of water inside it. This leads to the reconstitution of lyophilized NLCs, followed by the release of particles from the wafer into the artificial saliva as a release medium. Moreover, PVA is a water-soluble polymer, and through melt extrusion from the printing nozzle, it is converted into an amorphous form due to extrusion-mediated thermal shock, thereby improving the solubility of the printed matrix structure. Hence, particle release from 3D wafers in artificial saliva can be implemented in the treatment of oral cancer through localized buccal delivery of nanoparticles.

Conclusions

After the successful development of NLCs against oral cancer, there is a need for an advanced cutting-edge translational dosage form to deliver cargo at the local site of interest. PVA is a water-soluble polymer that can be easily 3D printed using its native filament. Initially, the wafer was designed using CAD software, and 3D printed using FDM-mediated 3D printing technology using a PVA filament. Physicotechnological evaluations were systematically performed for 3D wafers to measure the physical dimensions, surface morphology through optical microscopy and FESEM, and solid-state characterizations through DSC and XRD analyses. Specified dimensions with a smooth surface texture and a loading capacity of approximately 50 mg of NLCs made the complete translational form of the 3D wafer. The in vitro release of NLCs wrapped inside the 3D-printed wafers was experienced around 120 min in the presence of artificial saliva, which was validated through derived kCPS data obtained from the DLS study. Hence, 3D wafers can be a suitable substitute for other localized drug delivery systems to deliver the moiety of interest inside the buccal cavity.

Materials and methods

Materials

High-quality, natural polyvinyl alcohol (PVA) filaments (2.85 mm in diameter) were procured from Ultimaker, Germany. Compritol® 888 ATO, as a solid lipid, was obtained as a gift from Gattefosse, France. Active plant constituents, squalene (SQL) as a liquid lipid and sucrose as a cryoprotectant, were purchased from Sigma-Aldrich Chemical, St. Louis, MO. Sodium chloride, potassium hydrogen phosphate, potassium carbonate, calcium chloride dehydrate, magnesium chloride hexahydrate, sodium hydroxide, Tween 80, and Span 80 were purchased from HiMedia Laboratories Pvt. Ltd., Mumbai, India. Water

was purified with a Milli-Q & ELIX water purification system (Merck Millipore, USA) and used throughout the experiments.

Methods

Design of 3D wafers

Solidworks software (SOLIDWORKS-2019, US) as a computer-aided design (CAD) software was used to design the 3D-printed wafers and exported in the form of stereolithography (.stl) file into a 3D printer software (Ultimaker Cura Version 4.2.1, Singapore). The.stl file format comprises all the given printing parameters and surface data of the 3D-printed wafers needed for the 3D printer software to print the objects in the desired dimensions. The wafer was designed such that two parts would enclose a cavity fixed through screw-based projections using a lock-key system. The design of this 3D wafer was filed to an Indian Patent Office, and a favorable examination report has been generated on 27 May, 2021 [16].

Printing of 3D wafers

The.stl was converted into a G-code file containing geometric information for printing the 3D wafer. To print wafers as a 3D object, an FDM technology-based 3D printer (Ultimaker 3, Ultimaker, Germany) was implemented. High-quality natural PVA, a water-soluble polymer in the form of a filament, was used for the 3D printing process. Printing parameters such as printing speed, print layer height, and printing temperature were varied in different batches, as shown in Table 1. The diameter of the nozzle of the 3D printer was around 0.4 mm, assuring the fine printing through it.

Preparation and characterizations of NLCs

NLCs were synthesized using the solvent evaporation method, as previously reported. The homogeneous organic phase of a drug-lipid mixture containing Compritol® 888 ATO (solid lipid), squalene (liquid lipid), and active plant constituents (quercetin and piperine) were homogenized in an aqueous surfactant solution using a high shear homogenizer. Freeze drying of NLCs was performed using sucrose as a cryoprotectant using a lyophilizer (L-300, Buchi, Switzerland) [11].

Characterization of 3D wafers and NLCs

Physical appearance

To determine the shape, homogeneity, uniformity, and smoothness, all 3D-printed wafers were investigated visually [17].

Determination of physical dimensions

To characterize 3D wafers, physical dimensions such as length, width, and height were measured using a digital Vernier caliper (CD-6" ASX, Mitutoyo Corporation, Japan) [3, 17].

Determination of weight variation

Six randomly selected 3D wafers (with no NLC loading) from each batch were weighed individually on a digital single-pan balance (Mettler Toledo, Switzerland), and the average weight of the 3D wafers was calculated, which provides a clear-cut idea related to the weight variation among 3D-printed wafers.

Determination of loading capacity

The loading capacity of the 3D wafers was estimated by filling the lyophilized NLCs inside it, and then the wafers were fixed to each other with no leakage or spilling. Lyophilized NLCs were weighed in terms of their weight (in mg) on a digital single-pan balance (Mettler Toledo, Switzerland) and loaded with utmost care into the 3D-printed wafer. After proper loading of NLCs inside the 3D-printed wafer matrix, it was enclosed by a cavity fixed through screw-based projections using a lock-key system with proper fixation. After fixation of the entire assembly, the embedded NLCs were further subjected to in vitro NLCs release studies.

Microscopy of 3D wafers

Surface microstructural analysis of the 3D-printed wafer was performed using an inverted microscope (DMil, Leica, Germany). The upper and lower parts of the 3D wafer were sequentially placed on the coverslip and then visualized under the 10× and 4× objectives of the inverted microscope.

Scanning electron microscopy (SEM)

SEM is a technique used to determine the surface morphology of NLCs and 3D-printed wafers with the help of an electron beam under a vacuum. Hence, surface morphological evaluation of lyophilized NLCs and 3D-printed wafers was performed with field emission-SEM (FESEM, JSM-7610F, JEOL Japan).

Differential scanning calorimetry (DSC)

To determine the nature of the PVA filament and 3D wafer, DSC analysis was performed (DSC-3, Mettler Toledo, Switzerland). Approximately 5.0 mg of sample was placed in a sample pan and crimped with a crimping machine for tight sealing of the pan. The heating rate was maintained at 10 °C min⁻¹ within

the temperature range of 25–350 °C. Nitrogen purging was performed at 10 mL min⁻¹ flow rate to maintain a stable, inert atmosphere.

X-ray powder diffraction (XRD)

To determine the nature of the PVA filament and 3D wafer, XRD analysis was performed using a SmartLab diffractometer (Rigaku, Japan). Samples were sectioned as thin films and analyzed by keeping the constant parameters as applied voltage and applied current of 45 kV and 120 mA, respectively. The scan speed, omega, and step size were 4°/min, 1.0, and 0.02, respectively. The final data were plotted as 2θ values versus intensity.

Particle size analysis

The mean particle size and polydispersity index of the prepared NLCs were measured using a particle size analyzer (Nano-ZS, Malvern Instruments Ltd.).

Preparation of artificial saliva

Artificial saliva was prepared using a previously reported method, with some modifications [18]. Approximately 500 ml of deionized water was adjusted to pH 2.5 with the addition of concentrated hydrochloric acid (1.0 mL). Other components, such as sodium chloride (165 mg), potassium hydrogen phosphate anhydrous (340 mg), potassium carbonate (265 mg), calcium chloride dehydrate (75 mg), and magnesium chloride hexahydrate (85 mg), were weighed and solubilized in the previously prepared acidified water. The pH of the solution was adjusted to 6.8 ± 0.1, using 5 N sodium hydroxide solutions.

Determination of % redispersibility of NLCs

Redispersibility is the dispersion of lyophilized powder using a specific solvent. To restrict irreversible aggregation during lyophilization, a cryoprotectant must be added to the nanodispersion. Hence, the percent redispersibility of lyophilized NLCs was estimated in terms of the derived kCPS in artificial saliva. Approximately 1.0 ml of NLCs dispersion containing sucrose as a cryoprotectant was analyzed through DLS and then lyophilized the same sample using a lyophilizer (L-300, Buchi, Germany). After complete drying, the lyophilized NLCs were mixed with a similar volume of artificial saliva by vortexing for 5 min. The samples were then analyzed to determine the derived kCPS. Calculations were performed to estimate the % redispersibility of the lyophilized NLCs.

In vitro NLCs release study

The in vitro release profile pattern of the prepared lyophilized NLCs loaded into 3D-printed wafers was determined through photon count rate (in terms of derived kCPS measurement). Analysis of photon count rate is desired as it represents a

function of size and concentration of scattering particles [13]. Around 50.0 mg of Lyophilized NLCs were loaded inside the 3D-printed wafers, and an in vitro NLCs release study was performed in artificial saliva (pH 6.6) as a release medium at 37 ± 0.5 °C. At different time intervals, the whole medium containing released NLCs sample was removed and analyzed using DLS (ZetaSizer Nano-ZS, Malvern Instruments Ltd., UK) [12] with 4.0 mW He–Ne laser at 633 nm wavelength (red) as a plot of derived kCPS vs. time (min).

Acknowledgments

The authors would like to acknowledge the National Mission on Himalayan Studies (NMHS) [File No: GBPI/NMHS-2017-18/HSF-02], Ministry of Environment, Forest and Climate Change, Govt. of India to provide the necessary funding support for this research. Authors are also thankful to the Department of Pharmaceuticals, Ministry of Chemicals and Fertilizers, Govt. of India.

Data availability

The authors confirm that the data supporting the key findings can be made available upon request to the corresponding author.

Declarations

Conflict of interest The authors declare that there are no conflicts of interest.

References

1. A. Goyanes, U. Det-Amornrat, J. Wang, A.W. Basit, S. Gaisford, 3D scanning and 3D printing as innovative technologies for fabricating personalized topical drug delivery systems. *J. Control. Release* **234**, 41 (2016)
2. C.L. Ventola, Medical applications for 3D printing: current and projected uses. *Pharm. Ther.* **39**(10), 704 (2014)
3. U. Bhatt, T.K. Malakar, U.S. Murty, S. Banerjee: 3D printing of immediate-release tablets containing olanzapine by filaments extrusion. *Drug Dev. Indust. Pharm.* (2021). <https://doi.org/10.1080/03639045.2021.1879833>
4. A. Al-Taie, J. Pan, P. Polak, M.R. Barer, X. Han, A.P. Abbott, Mechanical properties of 3-D printed polyvinyl alcohol matrix for detection of respiratory pathogens. *J. Mech. Behav. Biomed. Mater.* **112**, 104066 (2020)
5. A. Goyanes, P.R. Martinez, A. Buanz, A.W. Basit, S. Gaisford, Effect of geometry on drug release from 3D printed tablets. *Int. J. Pharm.* **494**(2), 657 (2015)
6. A. Maroni, A. Melocchi, F. Parietti, A. Foppoli, L. Zema, A. Gazzaniga, 3D printed multi-compartment capsular devices for two-pulse oral drug delivery. *J. Control. Release* **268**, 10–18 (2017)
7. G. Matijašića, M. Gretić, J. Vinčić, A. Poropat, L. Cuculić, T. Rahelić, Design and 3D printing of multi-compartmental PVA capsules for drug delivery. *J. Drug Deliv. Sci. Technol.* **52**, 677–686 (2019)
8. T.K. Malakar, V.S. Chaudhari, S.K. Dwivedy, U.S.N. Murty, S. Banerjee, 3D printed housing devices for segregated compartmental delivery of oral fixed dose anti-tubercular drugs adopting print & fill strategy. *3D Print. Addit. Manuf.* (2021). <https://doi.org/10.1089/3dp.2021.0037>
9. V.S. Chaudhari, U.S. Murty, S. Banerjee, Lipidic nanomaterials to deliver natural compounds against cancer: a review. *Environ. Chem. Lett.* **18**, 1803–1812 (2020). <https://doi.org/10.1007/s10311-020-01042-5>
10. V.S. Chaudhari, P.K. Hazam, S. Banerjee, Lipid nanoarchitectonics for natural products delivery in cancer therapy, in *Sustainable Agriculture Reviews*, vol. 44 (Springer, Cham, 2020), pp. 169–203. https://doi.org/10.1007/978-3-030-41842-7_5
11. V.S. Chaudhari, U.S. Murty and S. Banerjee: Nanostructured Lipid Carriers as a strategy for encapsulation of active plant constituents: Formulation and in vitro physicochemical characterizations. *Chem. Phys. Lipids.* **235**, 105037 (2021)
12. R. Beck, P. Chaves, A. Goyanes, B. Vukosavljevic, A. Buanz, M. Windbergs, A. Basit, S. Gaisford, 3D printed tablets loaded with polymeric nanocapsules: an innovative approach to produce customized drug delivery systems. *Int. J. Pharm.* **528**(1–2), 268 (2017)
13. J. Smeraldi, R. Ganesh, J. Safarik, D. Rosso, Statistical evaluation of photon count rate data for nanoscale particle measurement in wastewaters. *J. Environ. Monit.* **14**(1), 79 (2012)
14. J. Norman, R.D. Madurawe, C.M. Moore, M.A. Khan, A. Khairuzzaman, A new chapter in pharmaceutical manufacturing: 3D-printed drug products. *Adv. Drug Deliv. Rev.* **108**, 39 (2017)
15. A. Goyanes, J. Wang, A. Buanz, R. Martinez-Pacheco, R. Telford, S. Gaisford, A.W. Basit, 3D printing of medicines: engineering novel oral devices with unique design and drug release characteristics. *Mol. Pharm.* **12**(11), 4077 (2015)
16. V.S. Chaudhari, T.K. Malakar, U.S. Murty, S. Banerjee: 3D Printed Mouth Dissolving Wafers: Application No. 342624–001. Cbr No. 202856, FER Issued: 27 May, 2021, Date of Filing: 22 April, (2021)
17. V.S. Chaudhari, T.K. Malakar, U.S. Murty, S. Banerjee, Extruded filaments derived 3D printed medicated skin patch to mitigate destructive pulmonary tuberculosis: design to delivery. *Expert Opin. Drug Deliv.* **18**(2), 301–313 (2021). <https://doi.org/10.1080/17425247.2021.1845648>
18. J.H. Miller, T. Danielson, Y.B. Pithawalla, A.P. Brown, C. Wilkinson, K. Wagner, F. Aldeek, Method development and validation of dissolution testing for nicotine release from smokeless tobacco products using flow-through cell apparatus and UPLC-PDA. *J. Chromatogr. B* **1141**, 122012 (2020)